

NPS ARCHIVE
1965
YOUNGMANN, K.

THE DESIGN AND DEVELOPMENT
OF A PRACTICAL EDGE SUPPORT FOR A
BILAMINAR DISK TRANSDUCER ELEMENT

KENNETH C. YOUNGMANN

DUDLEY KNOX LIBRARY
NAVAL POSTGRADUATE SCHOOL
MONTEREY CA 93943-5101

THE DESIGN AND DEVELOPMENT OF A PRACTICAL EDGE SUPPORT
FOR A BILAMINAR DISK TRANSDUCER ELEMENT

by

Kenneth C. Youngmann

Lieutenant, United States Navy

THE DESIGN AND DEVELOPMENT OF A PRACTICAL EDGE SUPPORT
FOR A BILAMINAR DISK TRANSDUCER ELEMENT

by

Kenneth C. Youngmann

Lieutenant, United States Navy

Submitted in partial fulfillment of
the requirements for the degree of

MASTER OF SCIENCE
IN
ENGINEERING ELECTRONICS

United States Naval Postgraduate School
Monterey, California

1965

DUDLEY KNOX LIBRARY
NAVAL POSTGRADUATE SCHOOL
MONTEREY CA 93943-5101

THE DESIGN AND DEVELOPMENT OF A PRACTICAL EDGE SUPPORT
FOR A BILAMINAR DISK TRANSDUCER ELEMENT

by

Kenneth C. Youngmann

This work is accepted as fulfilling
the thesis requirements for the degree of

MASTER OF SCIENCE

IN

ENGINEERING ELECTRONICS

from the

United States Naval Postgraduate School

ABSTRACT

A bilaminar disk has a low fundamental resonant frequency associated with small size. Application of this quality for practical transducers has been restricted due to the lack of suitable edge supporting devices for bilaminar disks. Various geometrical configurations for use as edge supports are considered in this report. Of these, it is concluded that a bilaminar disk supported above and below by a triangular ring will operate in the supported edge mode. Finally, the design, construction, and testing of a waterproofed bilaminar disk using triangular ring supporting devices is described.

The work presented here was performed at the Bendix-Pacific Division of the Bendix Corporation. I wish to express my gratitude to Mr. Gene Zilinskas of the Bendix Corporation for his guidance during the course of these investigations.

TABLE OF CONTENTS

Section	Title	Page
1.	Introduction	1
2.	Principle of bilaminar disk operation and construction details	2
3.	Preliminary tests	5
4.	Edge support design	8
5.	Test circuit for obtaining admittance curves	12
6.	Experimental results for the air support designs	13
7.	Water support design	18
8.	Measurements procedure for water tests	23
9.	Experimental results for the bilaminar disk transducer	27
10.	Conclusion	42
	Bibliography	
Appendix		
A	Outline of the analytical description of the bilaminar disk transducer	A-1
B	Sample calculations	B-1
C	Material properties of BaTiO_3 (5% CaTiO_3 additive) and summary of formulae and constants for the edge supported bilaminar disk transducer	B-1

LIST OF ILLUSTRATIONS

Figure	Title	Page
1a	Cross section of a typical bilaminar disk	2
1b	Dimensions and electrical connections of the bilaminar disk	2
2	Stages of element construction (Photo)	4
3	Test circuit for obtaining admittance amplitude	5
4	Boraxo powder defining nodal locations (Photo)	7
5a	Mounting block used for air measurements	9
5b	Mounting devices designed	10
6	Mounting block and supporting devices (Photo)	11
7	Block diagram of the test circuit used for obtaining admittance curves	12
8	Admittance curves for various mounting configurations	14
9	Typical admittance curve for the triangular ring mount	16
10	Schematic of waterproofed unit	19
11a	Mounting devices used in the waterproofed unit	20
11b	Hardware used for varying the oil volume in the waterproofed unit	20
12a	Complete water unit (Photo)	21
12b	Supporting devices used in the water unit (Photo)	22
12c	Hardware used for varying the oil volume	22
13	Bridge circuit used for admittance measurements	23
14	Block diagram of the transmit/receive circuit used for T_A determination	24
15	Block diagram of the receiving portion of the pattern making circuit	26
16	Conductance curves for tests 1a, 1b, and 2	32
17	Azimuth receive pattern for test 1a. Recorded at 7.35 Kcps	33
18	Azimuth receive pattern for test 2. Recorded at 7.25 Kcps	34

Figure	Title	Page
19	Transmit pattern for 20 watts of input power. Recorded at 7.3 Kcps	35
20	Conductance curves for tests 4 and 5	36
21	Azimuth receive pattern for test 4. Recorded at 5.75 Kcps	37
22	Azimuth receive pattern for test 5. Recorded at 5.8 Kcps	38
23	Conductance curves for tests 6 and 7	39
24	Azimuth receive pattern for test 6. Recorded at 5.7 Kcps	40
25	Azimuth receive pattern for test 7. Recorded at 5.75 Kcps	41
A1	Electromechanical circuit of a bilaminar disk	A-8
B1	Azimuth receive pattern for a bilaminar disk. Recorded at 7.25 Kcps	B-4
B2	Plot of p^2 versus θ (Required for obtaining the directivity index)	B-5
B3	Conductance curve for the bilaminar disk transducer	B-6
B4	Susceptance curve for the bilaminar disk transducer	B-7

Table

1	Results of preliminary tests in air for the free-free disk and the disk supported at its edges by triangu- lar rings	17
2	Identification of water tests	27
3	Experimental results and index to Figures 17-25	28
4	Results of test 3, determination of maximum input power	30

SYMBOLS

a	Radius of the bilaminar disk
A	Admittance amplitude
A_1	Area of the bilaminar disk
B	Parallel susceptance of the bilaminar disk
b	Thickness of the bilaminar disk
c_p	Sound velocity of extensional waves in an infinitely extended medium
C_B	Blocked capacitance of the bilaminar disk
C_C	Parallel capacitance of the transducer cable
C_D, C_P	Parallel capacitance of the bilaminar disk as measured on an a/c bridge
C_M^E	Compliance of the bilaminar disk at constant voltage
C_c	Series equivalent of C_C
D_3	Electric displacement in the x_3 direction
d	Transducer to calibrated hydrophone distance
DI	Directivity index
dA_1	Element of area of the bilaminar disk
dS	Element of spherical surface area
E_D	The rms voltage across the disk transducer
E_D'	The peak to peak value of E_D
E_S	The rms voltage across the calibrated hydrophone
E_S'	The peak to peak value of E_S
e	The electric potential applied to the disk
\mathcal{E}_3	The electric field in the x_3 direction
F	Frequency expressed in Kcps
f_{ra}	Resonant frequency of the unloaded disk

f_{rw}	Resonant frequency of the water loaded disk
G	Parallel conductance of the disk
g_{31}	Piezoelectric strain constant
H	Constant defined by equation A-23a
I_D	Rms current in to the disk transducer
I'_D	The peak to peak value of I_D
j	Imaginary unit
k	Electromechanical coupling coefficient
k_p	Planar electromechanical coupling coefficient
M	Equivalent mass of the bilaminar disk
M_S	Sensitivity of the calibrated hydrophone expressed in decibels re 1 volt rms per microbar
N	Transformer turns ratio
$p(\phi, \theta)$	The sound pressure as a function of direction at some fixed distance
p_a	The sound pressure in the reference direction at the fixed distance determined by $p(\phi, \theta)$
Q_E	R_p / X_p
Q_M	Mechanical quality factor
R_B	Bridge resistor
R_P	Parallel resistance of the bilaminar disk as recorded on an a/c bridge
R_S	Series equivalent of R_P
R_1, R_2	Principal radii of curvature of the disk
R_0	Directivity factor
r	Radial coordinate
S_s	Sensitivity of the calibrated hydrophone expressed in rms volts/microbar
S_o	Transmit current response expressed in microbars/ampere at 1 meter

D_{s11}	Compliance modulus at constant electric displacement
t	Time
T_A	Transmit current response expressed in decibels re 1 microbar/ampere at one meter
T_P	Kinetic energy of the disk
T_i	Extensional stresses
T_{ij}	Shear stresses
T_W	Kinetic energy in the near field of a single disk
U_A	Strain energy per unit area
U_V	Strain energy density
U_e^W	Blocked electrical energy of the disk
U^E	Potential energy of the disk at constant voltage
U^I	Potential energy of the disk at constant current
u_{av}	Reference displacement
$u(r)$	Normal displacement of the central surface of the disk
v	Reference velocity
X_P	Parallel reactance of the bilaminar disk
x_3	Rectangular coordinate
$\alpha_0, \dots, \alpha_4$	Deflection curve coefficients
β_{33}^T	Dielectric impermeability at constant stress
$\beta_{33}^{\alpha_{1,2}}, \beta_{33}^{\alpha_{1,2}}$	Impermeability for a disk blocked at its edges
η	Electromechanical efficiency
η_{db}	$10 \log \eta$
Θ	Constant defined by equation A-31a
θ	angular coordinate
\mathcal{K}	Constant defined by equation A-5a
\mathcal{L}^D	Constant defined by equation A-16a

Λ^E	Constant defined by equation A-17a
Λ^T	Constant defined by equation A-17b
Ξ	Amplitude of ξ
γ	Time varying amplitude factor
ρ_p	Density of the disk material
ρ_p^e	Effective density of the bilaminar disk
ρ_w	Density of water
σ^D	Poisson's ratio of piezoelectric material at constant D_3
ψ	Phase angle between I_D and E_D
ω	Angular frequency

Section 1. Introduction.

The development of a bilaminar disk transducer presents a method for the miniaturization of transducer elements. One of the main reasons that these elements have not been extensively used lies in the difficulty in meeting the boundary conditions specified by the design equations.

Woollett's paper derives the design equations for the clamped edge, the supported edge, and the supported center modes of operation [7]. The clamped edge has a theoretically zero electromechanical coupling coefficient, and hence, is not desirable for transducer use. The center support configuration has a respectable electromechanical coupling coefficient. However, waterproofing a center support mount requires the elimination of viscous damping at the edge of the disk. The edge support mount has the highest electromechanical coupling coefficient of the three modes, and there is no viscous damping problem. Therefore, the development of a true edge support will allow the optimum use of a bilaminar disk.

This report, then, is primarily concerned with the development of an edge support for a bilaminar disk. The primary design consideration is resonant frequency. However, efficiency, bandwidth, and beam patterns will be determined experimentally as indicators of the design's usability. This paper describes the support mounts designed, constructed, and tested. Test procedures are given when appropriate. The relevant theory is given in the appendices.

Section 2. Principle of bilaminar disk operation and construction details.

The transducer elements studied in this report were composed of BaTiO_3 with a 5% CaTiO_3 additive. The wafers have a polarization vector normal to their major surfaces, and have silver electrodes deposited on their major faces. Two wafers are bonded together so that their inner faces are in electrical contact and their polarization vectors are aligned, thus forming a bilaminar disk. Figure 1a represents a cross section of a typical bilaminar disk.

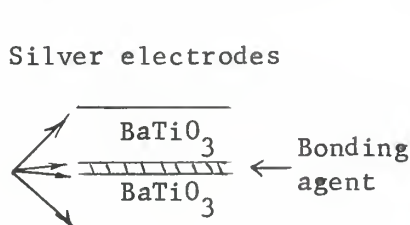


Figure 1a.
Cross section of a typical bilaminar disk.

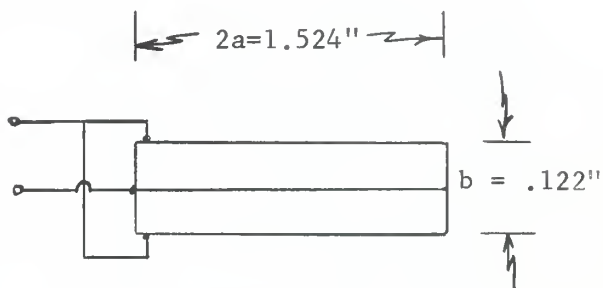


Figure 1b.
Dimensions and electrical connections of the bilaminar disk.

Application of an electric field in the direction of polarization causes a planar contraction normal to this direction. Similarly an electric field applied in the opposite direction causes a planar expansion. From Figure 1b it is seen that the wafers of a bilaminar disk have electrical connections such that one wafer expands while the other wafer contracts when the disk is electrically excited. The bonding agent prevents slipping at the interface so that the bilaminar disk bends toward the wafer subject to the planar compressive forces. It is concluded then, that under the excitation of a sinusoidal field, the bilaminar disk becomes a flexural vibrator [6] .

The transducer element's dimensions and electrical connections are shown in Figure 1b, and the various stages of construction are shown in Figure 2. In the first set of elements constructed, Shell Chemical Company's Epon VI, an epoxy compound, Eastman's 910, a contact cement, and Armstrong's A-2 adhesive were used as bonding materials. By exciting these elements in the test circuit of Figure 3, and noting the change in admittance from resonance to antiresonance, it was determined that the Epon VI and the A-2 elements were far more responsive than the Eastman 910 elements. By a similar experiment, it was determined that the change in admittance from resonance to antiresonance was independent of bonding pressure for pressures greater than 2.5 pounds per sq. in. for both the Epon VI and A-2 elements. Furthermore, response was a maximum in this range of bonding pressures. Finally, Epon VI was chosen as the bonding agent for all elements to be constructed in the future since its excess after curing could be removed from the disk edges easier than the A-2.



(a) Silver plated disk.



(b) Silver tab location.



(c) Bonded disk.



(d) Completed disk.

Figure 2. Stages of element construction.

Section 3. Preliminary tests.

Before trying various mounting configurations, it was necessary to be able to identify the various modes of vibration when they occurred. The technique used by Zilinskas in his experiments with bilaminar bars was attempted here and found to be successful [8]. This technique involved sprinkling powder (in this case Boraxo Powdered Hand Soap was ideal) on the face of the vibrator and then resonating the element. The powder would then collect at the nodes so as to define the nodal locations. In the notation of Kinsler and Frey, the f_{02} and f_{03} modes were identifiable for a free disk, and the f_{01} mode was visible for the supported disk [4]. The pictorial results are given in Figure 4, and the numerical results are given in Table 1 on page 17 of this report. It should be noted that the frequency of the f_{03} mode for the free disk is predictable in accordance with the derivation for the asymmetrical free vibrations of a circular membrane as given by Kinsler and Frey.

The test circuit for these preliminary tests was merely a low impedance source driving the element and a ten ohm series resistor. See Figure 3. From this circuit admittance amplitude can be determined.

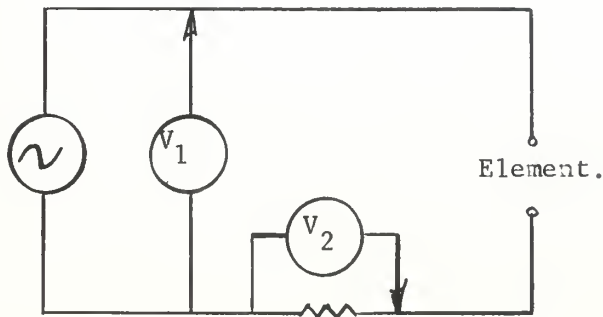


Figure 3.
Test circuit for obtaining admittance amplitude.

At this point it is convenient to define the term activity as "The change in admittance amplitude from resonance to antiresonance expressed in decibels referenced to 1 micromho." This term is useful when expressing how "active" an element is and will be used in the remainder of this report.



(a) Free disk, f_{02} mode.



(b) Free disk, f_{03} mode.



(c) Supported disk, fundamental mode.



(d) Ball bearing supported disk, triangular pattern near 17 Kcps.

Figure 4. Boraxo powder defining nodal locations.

Section 4. Edge support design.

It was felt that by finding an edge support that works in air, that this same design would operate when the element was waterproofed. Furthermore, elements can be mounted and tested with more facility in air than in water.

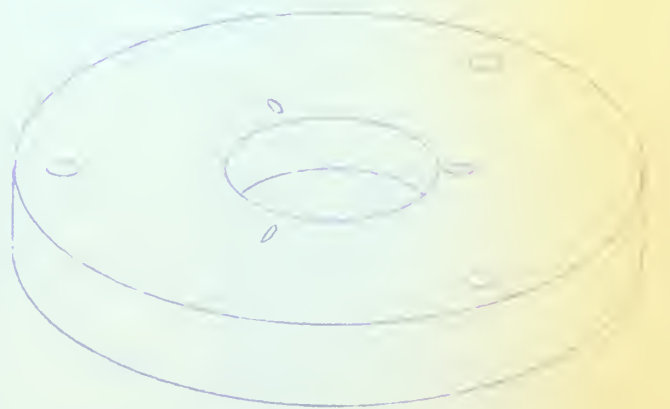
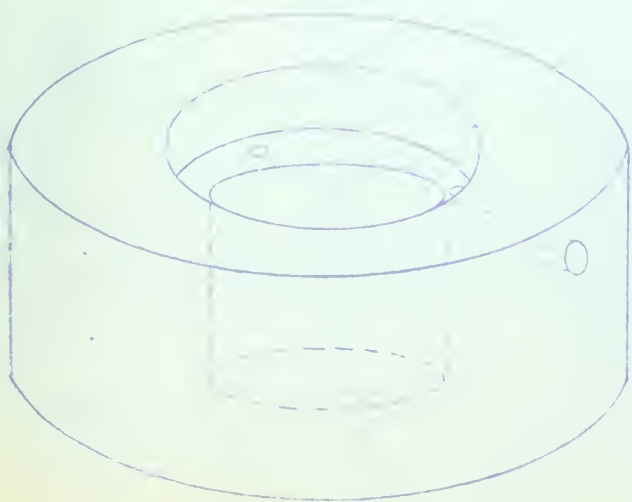
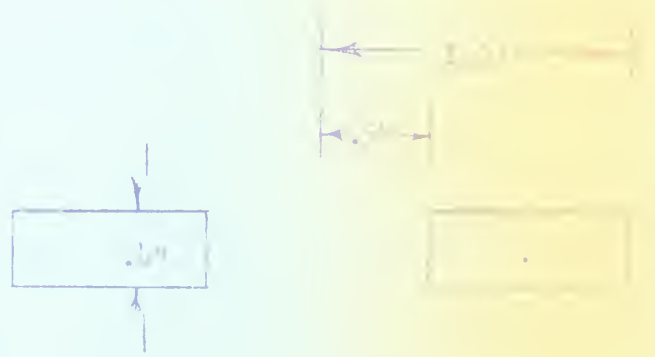
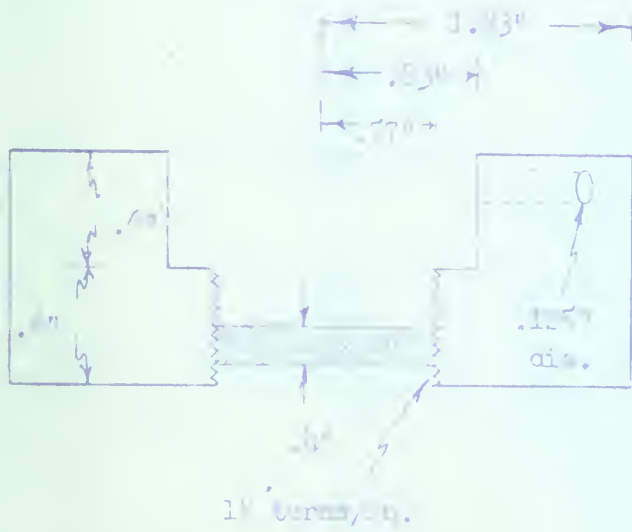
The basic design concept is summarized by this quote from Woollett's report.

..., the guiding principle in the design of edge supports must be to avoid radial blocking; unless each lamination is free (from external restraints) to expand or contract radially in response to the piezoelectric forces, no bending will develop (i.e., we will have retrogressed to the clamped edge case).¹

With this principle as a guide, an aluminum mounting block was designed to which various steel mounting devices could be attached. Initially, several geometric configurations were designed as mounting devices. These designs and the hardware constructed are shown in Figures 5 and 6, respectively.

These devices are to support the disk at its upper and lower surfaces, so their diameter must be somewhat smaller than the disk diameter. The support diameter chosen was 1.4 inches, or 92% of the disk diameter. From formula A-32, it appears that this reduced diameter will cause a slight increase in the fundamental resonant frequency. Test results showed this statement to be true.

1 Woollett, R. S. Theory of the Piezoelectric Flexural Disk Transducer, with Applications to Underwater Sound, USL Research Report No. 490, Dec., 1960: p.41



Bottom section.

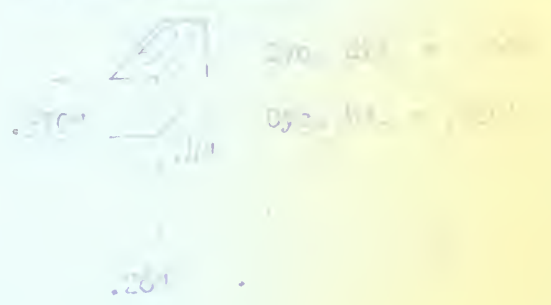
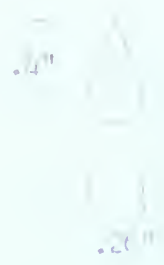
Top section.

Figure 50a Rotating block used for air bearings.

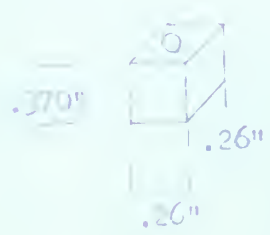


Point:

Roller cylinder:



Ball bearing:



Ball bearing 3/8" = .375
Total ht. = .4"

Triangular ring:



Match for wires.

Cross section.

Figure 5b. Mounting devices designed.



(a) Ball bearing supports.

(b) Triangular ring support.

(c) Wedge supports.



(d) Mounting block, top half.



(e) Mounting block, bottom half.

Figure 6. Mounting block and supporting devices.

Section 5. Test circuit for obtaining admittance curves.

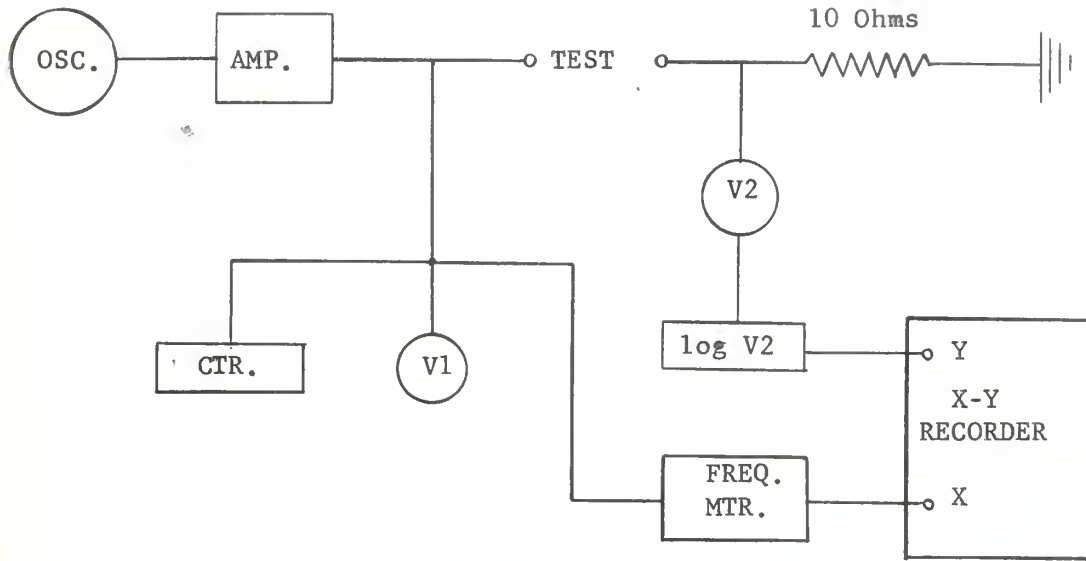


Figure 7.

Block diagram of test circuit used for obtaining admittance curves.

Principle of operation:

The output of V2 is a voltage proportional to the element's admittance amplitude and is directed into a log voltmeter whose output is a DC voltage proportional to the log of the input voltage. This signal is then fed to the Y axis input of the X-Y recorder. Then a sample of the signal sent to the test element is directed into a frequency meter whose output is a DC voltage proportional to the input frequency. This voltage becomes the X axis input of the X-Y recorder. The X-Y recorder is then scaled to present a plot of $20 \log A$ versus F . Here A is the admittance amplitude expressed in micromhos and F is frequency expressed in kilocycles per second.

Section 6. Experimental results for the air support designs.

The mounting devices shown in Figure 6 were placed in the test circuit of Figure 7. Boraxo powder was placed on each element in order to visually confirm the support mode when it occurred. When a support mode occurs, the nodal line (zero vertical motion) is along the edge of the disk and the Boraxo will collect along this line. Finally, the element was driven at 10 volts and the frequency was varied from 2 to 20 kilocycles.

Ball bearing mount.

The ball bearing mount gave a fundamental resonance near 6 Kcps. At this frequency, the Boraxo powder shifted randomly and no nodes were indicated. However, the admittance curve for this frequency proved that this was a pure resonance. See Figure 8. Any practical use of this mounting configuration is severely limited by the disk's tendency to crack at the points of contact with the ball bearings.

It is interesting to note the resonance at 17 Kcps for the ball bearing mount. At this frequency the Boraxo formed an equilateral triangle with an apex at each of the ball bearings. See Figure 4. The three segments so formed were vibrating out of phase with the center triangle. This indicates that this mode is inefficient and hence is impractical for transducer use. Further description of this result is beyond the scope of this report.

Wedge support mount.

The wedge supported disk behaved in a manner quite similar to the ball bearing supported disk. A description of these results would be repetitive.

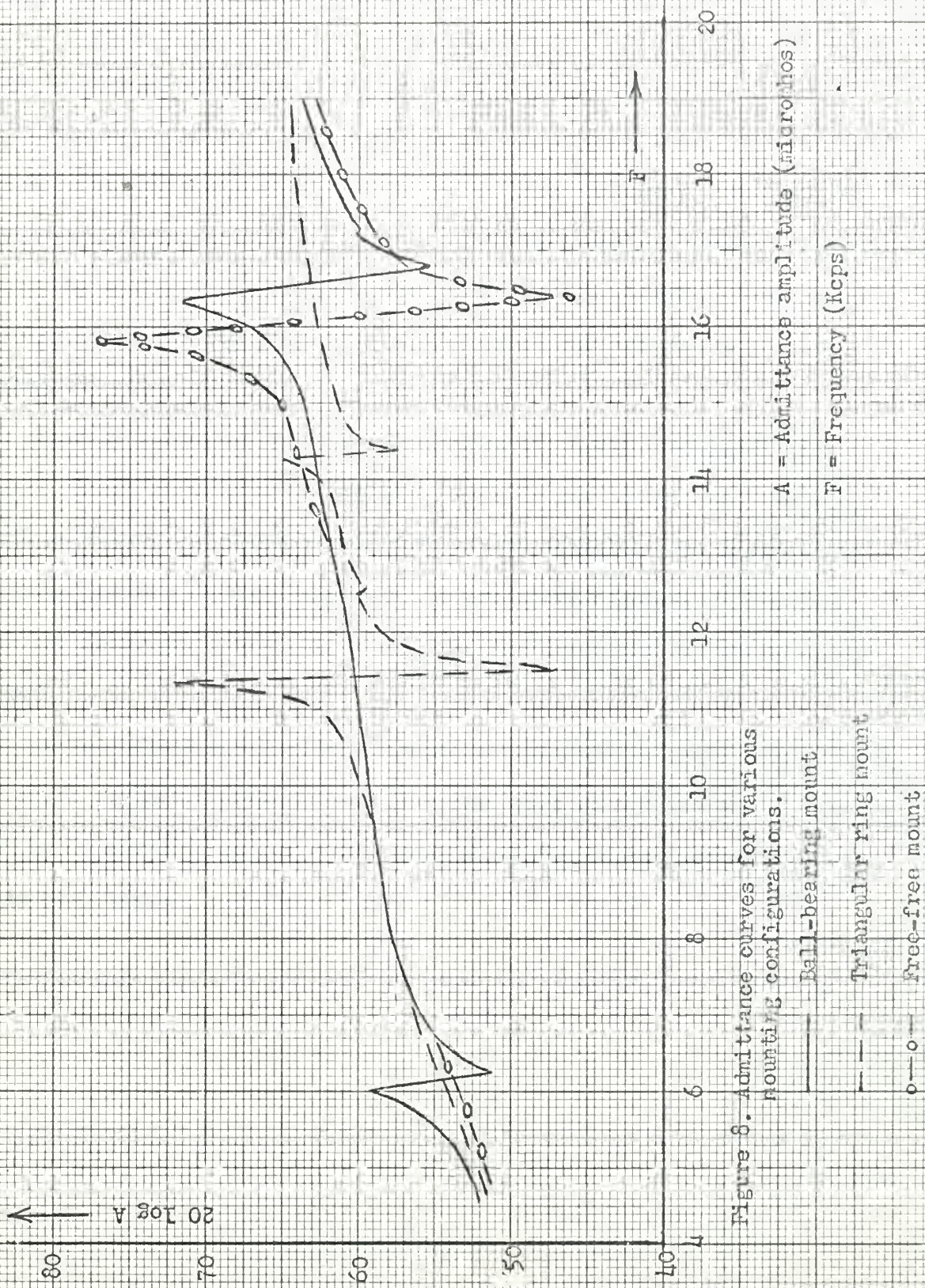


Figure 8. Admittance curves for various mounting configurations.

A = Admittance amplitude (microhms)
 F = Frequency (Kcps)

- Ball-bearing mount
- - - Triangular ring mount
- o - o - Free-free mount

Triangular ring support.

The disk supported by a triangular ring had a fundamental resonance near 11 Kcps and the Boraxo collected at the edge of the disk. This indicated that the disk was operating in the support mode. The admittance curve confirmed a pure resonance at this frequency. To confirm the support mode, a disk was clamped by brass rings and tested. Absolutely no activity was observed when the disk was clamped. From these results it is concluded that the support mode was achieved with the triangular ring.

Several different elements were operated in the triangular ring mount. Their admittance curves were taken by use of the test circuit shown in Figure 7. These curves were almost identical and Figure 9 is a typical curve. Table 1 compares the predicted resonant frequencies with the observed values. It also gives the activities of the elements tested.

It was concluded that the triangular ring mount closely approximates the ideal support configuration. The next step in the process of development is to design a waterproofed mount using the triangular ring as the supporting device.

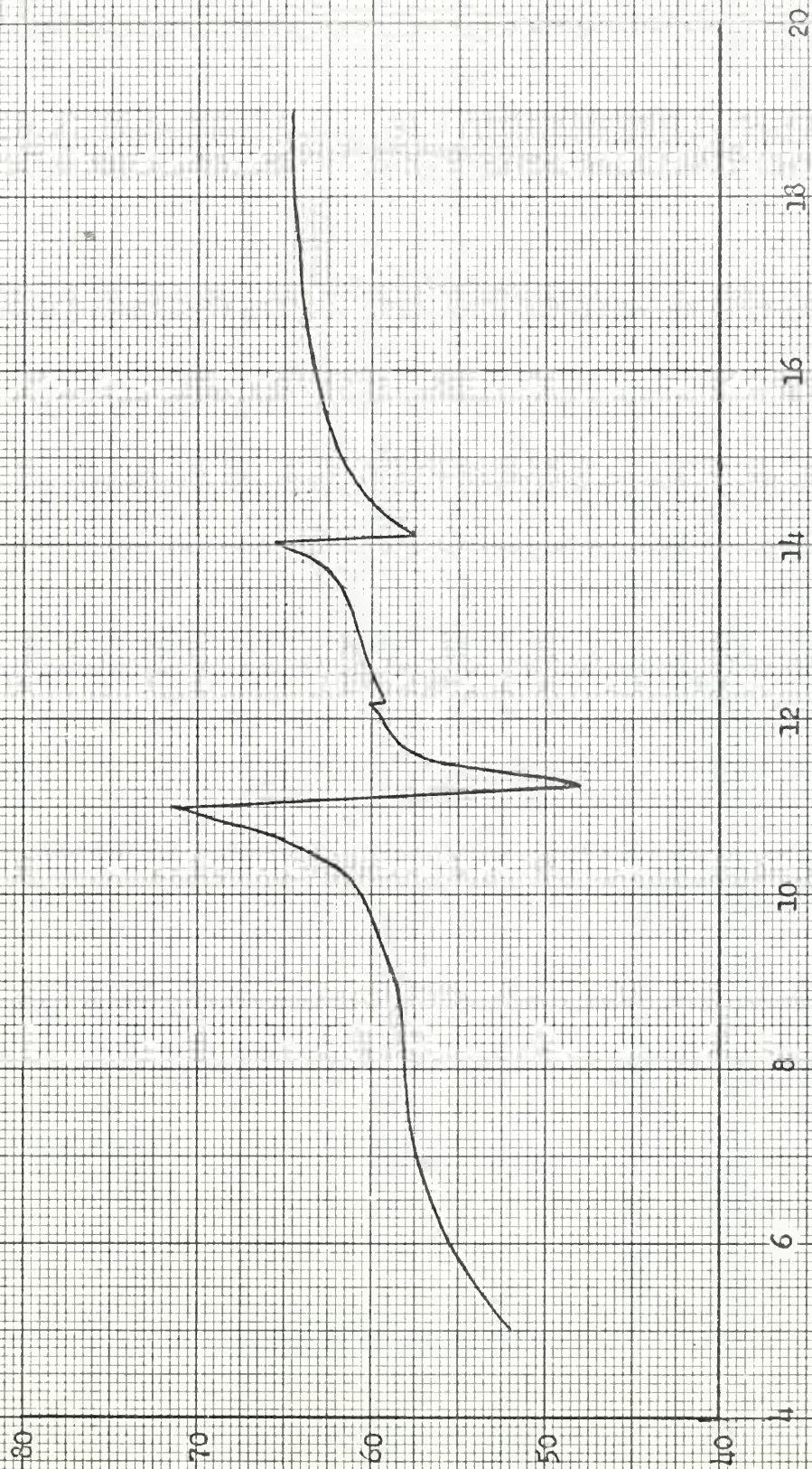


Figure 9. Typical admittance curve for triangular ring mount.

A = Admittance amplitude (microhos)

F = Frequency (Kcps)

Disk #	Free-free disk			Supported-edge disk		
	f_{ra}^* (predicted)	f_{ra} (observed)	Activity (db re 1 micromho)	f_{ra}^{**} (predicted)	f_{ra} (observed)	Activity (db re 1 micromho)
1	16.9 kcps	16.06 Kcps	28.5	10.7 Kcps	11.48 Kcps	24.7
2	"	16.09	31.9	"	11.67	26.8
3	"	15.84	29.8	"	11.61	26.9
4	"	15.76	23.3	"	-----	-----
5	"	16.30	26.5	"	11.44	24.5
6	"	16.14	26.7	"	11.47	25.3

Table 1

Results of preliminary tests in air for the free-free disk and the disk supported at its edges by triangular rings.

* f_{ra} for the free-free disk is predicted by equation A-37.

** f_{ra} for the supported edge disk is predicted by equation A-18.

Section 7. Water support design.

Since the triangular ring mounting device performed so well in air, it was decided to use it in a waterproofed unit. The mounting structure was designed to allow for the variation of mounting devices should the triangular ring be impractical as a waterproofed supporting device. Castor oil was chosen as the coupling compound rather than a polyethane compound since it was foreseen that it would be necessary to open the case for changes such as changing disks. Initially the volume of oil in back of the element was that of a cylinder whose diameter is equal to the diameter of the triangular ring support and whose height corresponded to one half of a wavelength of sound at the predicted fundamental resonance of 7.79 Kcps. See formula A-32. However, it should be noted that this is not the exact geometric configuration of the oil volume. Since the mount was constructed of pure metal, it was necessary to etch the silver from the edge of the disk in order to electrically isolate the disk from the case. Admittance measurements proved that this etching did not affect the acoustic properties of the transducer.

After determining that this mount was actually a waterproofed support (see results in the next section of this report), it was decided to vary the volume of oil in back of the element so that the mount might eventually be miniaturized. The mounting case is shown in Figure 10, and the supporting devices and the hardware for varying the oil volume in back of the element are shown schematically in Figures 11a and 11b, respectively. Figures 12a, 12b, and 12c are photographs of the actual hardware constructed.

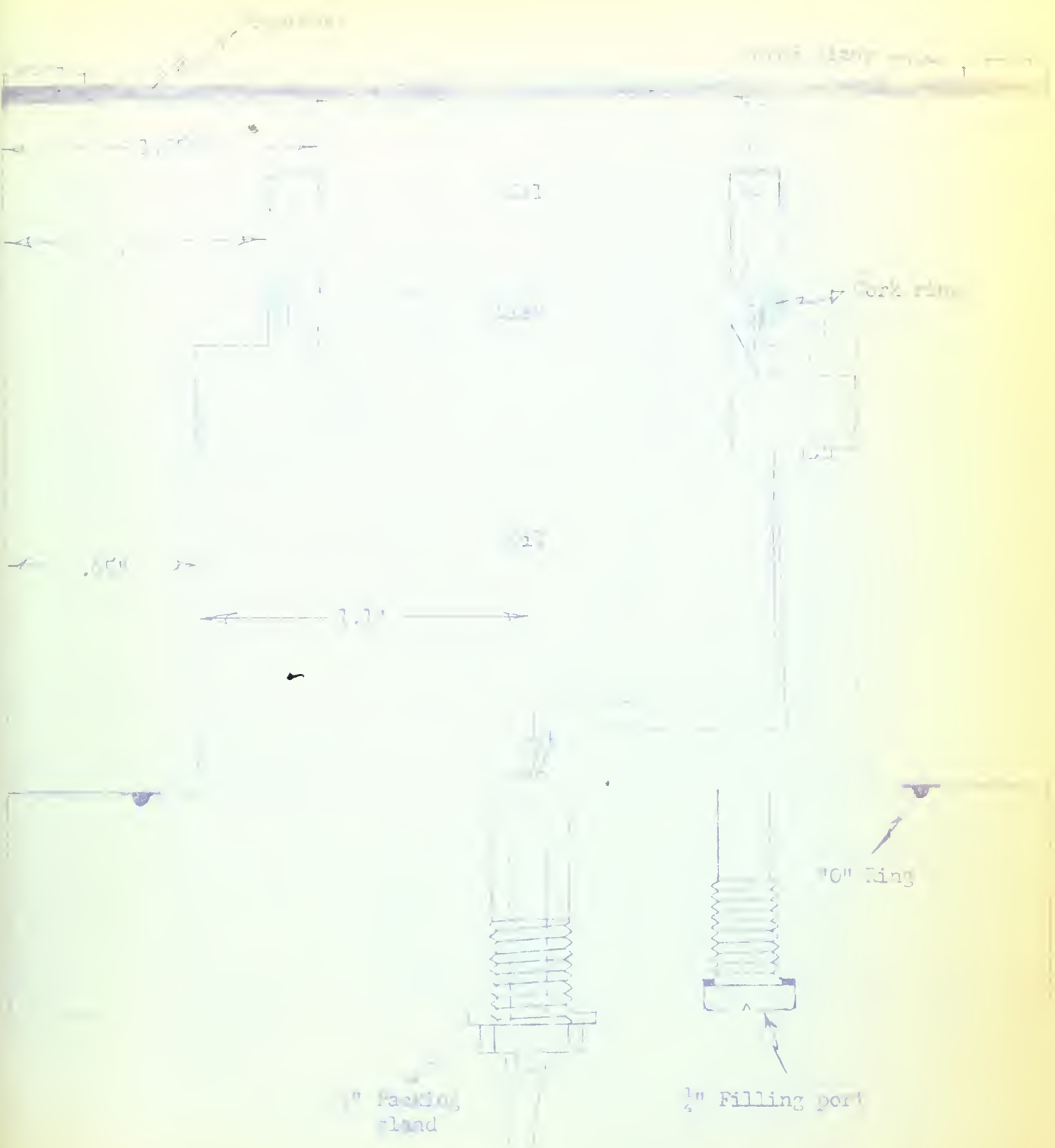


Figure 10. Assembly of water-tight joint.

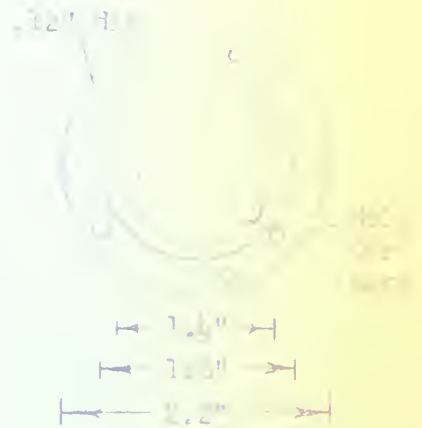
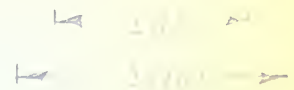
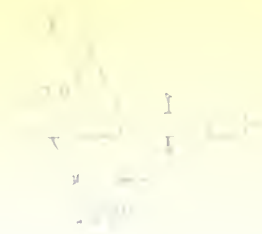


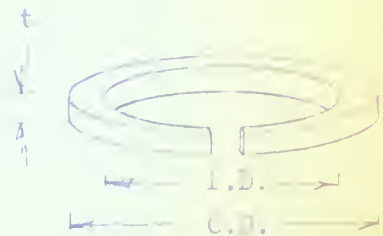
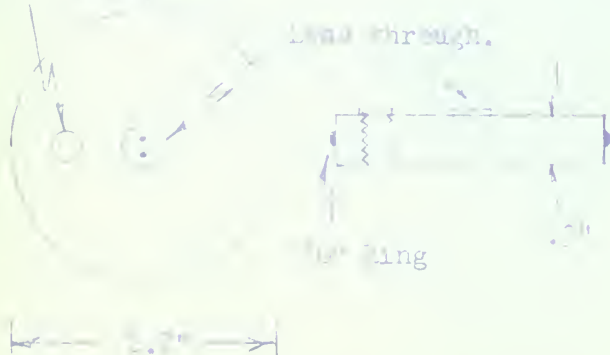
Figure 11a. Mounting devices used in waterproofed unit.

Figure

Spacing rings:

1/2" filling part.

Lead through.



Quantity	I.D.	O.D.	t
1	2"	2.2"	.3"
2	2"	2.2"	.3"
1	2"	2.2"	.3"

Figure 11b. Spacing rings used for varying the oil volume in waterproofed unit.



FIGURE 12 a COMPLETE WATER UNIT

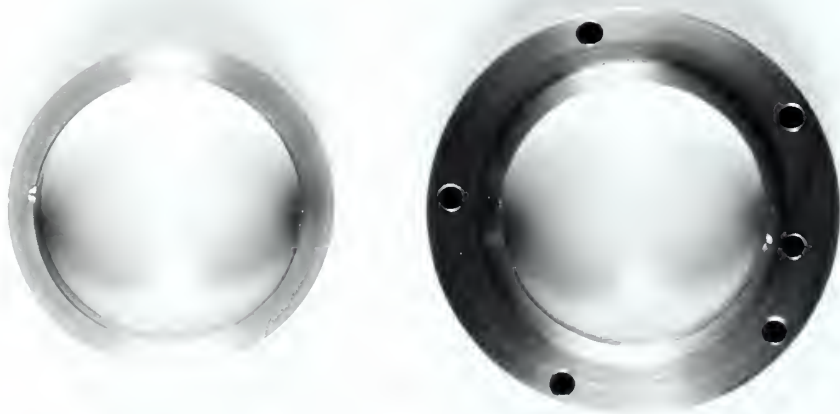


Figure 12b. Supporting devices used in water unit.



Figure 12c. Hardware used for varying oil volume.

Section 8. Measurements procedure for water tests.

All water tests on the bilaminar disk transducer were made in a rectangular, concrete, test tank. The tank is 30' long, 15' wide, and 15' deep at its sides. Its bottom is wedge shaped, with the apex of the wedge 13' below the surface and running the length of the tank. The purpose of the wedge is to increase the travel time of bottom reflections. The bilaminar disk transducer was placed in the center of the tank at a depth of 6'. When a calibrated hydrophone was used, it was placed in the center of the tank at a depth of 6' and 3 meters from the disk transducer. In all tests the applied signal was a one millisecond pulse used at the rate of 10 pulses per second.

Admittance measurements were made over the frequency range of 4 to 16 Kcps. using the bridge circuit shown in Figure 13. The data recorded after balancing was equivalent to the transducer's parallel resistance R_p and parallel capacitance C_p . These values were converted to equivalent parallel conductance G and parallel susceptance B .

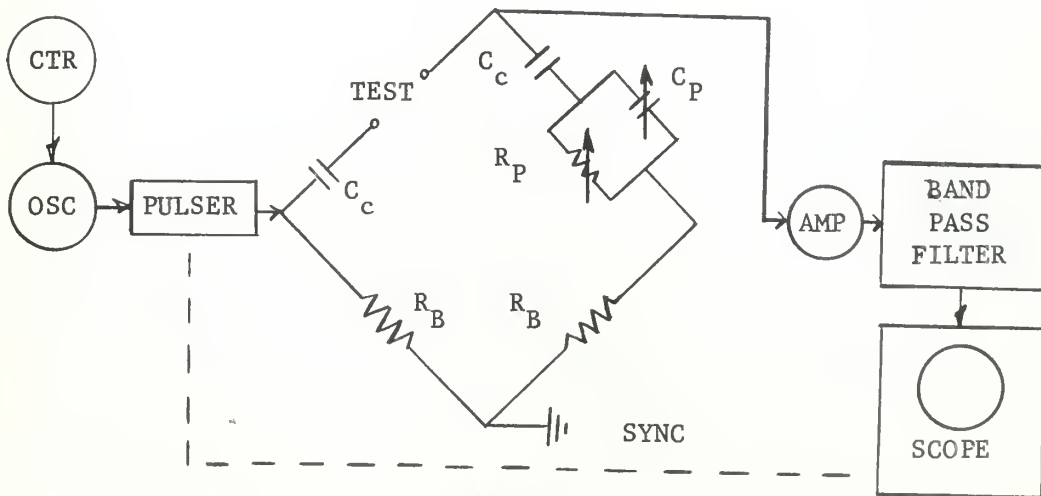


Figure 13
Bridge circuit used for admittance measurements.

The first part of the experiment was to determine the effect of the concentration of the solution on the rate of reaction. The rate of reaction was measured by the volume of gas evolved over a period of time. The results are shown in the following table.

Concentration of Solution	Volume of Gas Evolved (cm ³)	Time (s)	Rate of Reaction (cm ³ /s)
0.1 M	10	100	0.1
0.2 M	20	100	0.2
0.3 M	30	100	0.3
0.4 M	40	100	0.4
0.5 M	50	100	0.5

The results show that the rate of reaction increases linearly with the concentration of the solution. This is because there are more particles available to react, leading to a higher frequency of collisions.



Figure 13: Diagram of the apparatus used for measuring the rate of reaction.

In Figure 13 the following symbols apply

C_c = the series equivalent capacitance of the transducer cable,

R_B = the bridge resistor,

C_p = the parallel capacitance of the transducer, and

R_p = the parallel resistance of the transducer.

The test circuit shown in Figure 14 was used to determine the transmit current response, T_A , of the bilaminar disk transducer. By

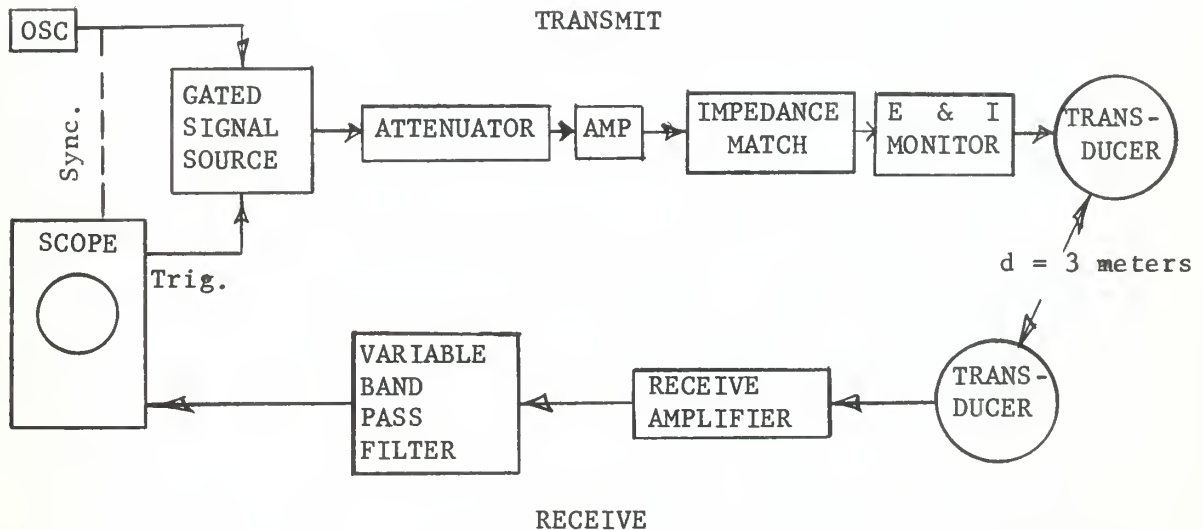


Figure 14

Transmit/Receive circuit used for T_A determination.

knowing the sensitivity of the receiving transducer, the transmit current response is found as follows:

$$T_A = 20 \log_{10} E_s - S_s + 20 \log_{10} d - 20 \log_{10} I_D$$

where,

E_s = rms voltage across the calibrated receiving transducer,
 S_s = the sensitivity of the receiving transducer expressed in
decibels referenced to one volt/microbar,
 I_D = the rms current flowing into the bilaminar disk transducer,
and,
 d = the transducer separation expressed in meters.

The correction for the cable capacitance is described in Appendix B.

When the input power is greater than two watts, a 32 millihenry tuning inductor and a one ohm resistor are placed in series with the bilaminar disk transducer. The tuning inductor reduces the phase angle between the current and voltage so that a high power source will not be required to drive the transducer. The one ohm resistor allows the input current to be monitored. A dual trace oscilloscope is used to determine the phase angle, the voltage across each transducer, and the current into the bilaminar disk transducer. This data can then be used to calculate efficiency for high input power as described in Appendix B.

The transmitting circuit used for pattern making is the same as that shown in Figure 14. Figure 15 shows the receiving portion of the pattern making circuit. It is interesting to note that by use of the gating element in the receive circuit that any portion of the received signal can be used to drive the pattern recorder. This eliminates any interference due to reflections. For all patterns in this report the 0 db. level is taken to be that of maximum response.

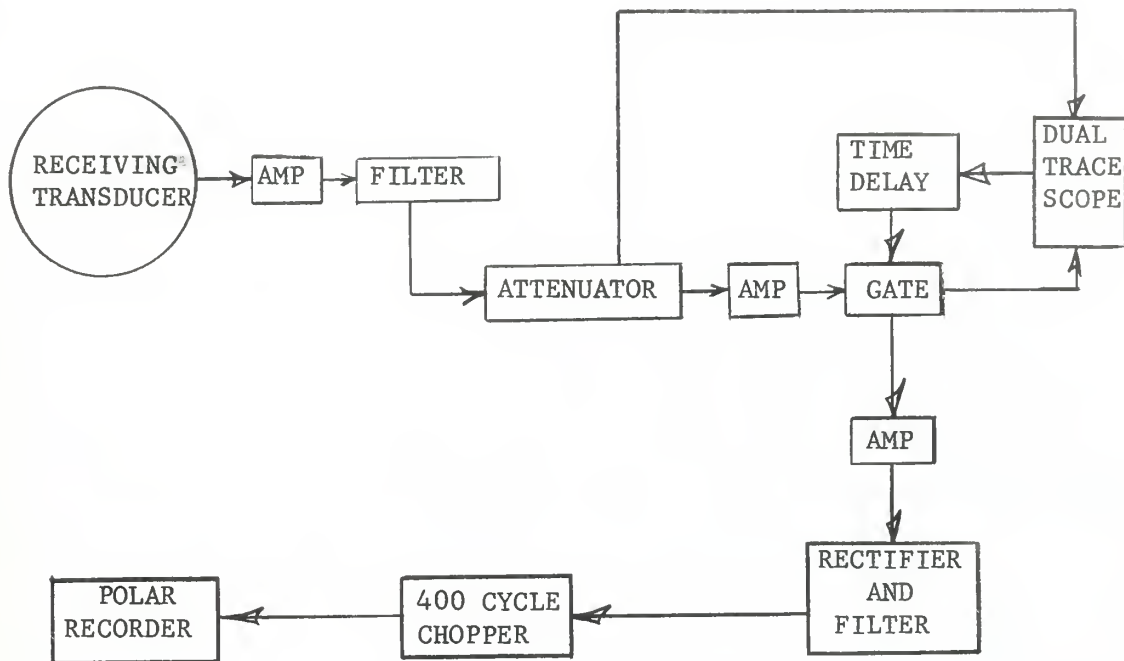


Figure 15

Block diagram of the receiving portion on the pattern making circuit.

Section 9. Experimental results for the bilaminar disk transducer.

Experimental data were obtained by use of the test circuits described in the preceding section. Initially, the transducer was operated with the rear cavity completely oil filled. Additional tests were conducted for various increments of rear cavity oil volume. Primary test objectives were a determination of resonant frequency, i. e., the frequency of maximum conductance, efficiency, and the maximum input power. The transducer's series resistance, R_S , directivity index, DI, mechanical quality factor, Q_M , conductance curve, and susceptance curve are also derived from the experimental data. Table 2 describes each test and Table 3 presents the recorded data and calculated results.

Test #	Disk #	Oil cavity volume	Predicted f_{rw}^*	Input power
1a	1	1.50π in. ³	7.79 Kcps	Less than 2 watts
1b	1	"	"	" " 2 "
2	2	"	"	" " 2 "
3	1	"	"	Power test-see below
4	2	0.33π	---	Less than 2 watts
5	2	0.53π	---	" " 2 "
6	2	0.77π	---	" " 2 "
7	2	0.90π	---	" " 2 "

Table 2

Identification of water tests.

* f_{rw} is predicted by equation A-32.

Test #	f_{rw} (Kcps)	T_A^*	R_S (ohms)	DI	(%)	Q_M	Transmit/Receive Pattern	Conductance Curve
1a	7.35	94.5	219	6.5	26.9	4.5	Figure 17	Figure 16
1b	7.60	91.4	246	6.3	12.0	6.2	Identical to Figure 17.	Figure 16
2	7.25	93.7	255	5.5	23.4	4.3	Figure 18	Figure 16
3 ^{**}	-	-	-	5.5	-	-	Figure 19	-
4	5.90	86.8	299	2.6	8.1	4.5	Figure 21	Figure 20
5	5.80	82.9	275	2.1	4.0	4.3	Figure 22	Figure 20
6	5.70	105.0	365	2.6	-	5.7	Figure 24	Figure 23
7	5.80	87.5	176	2.2	17.4	3.8	Figure 25	Figure 23

Table 3. Experimental results and index to figures 17 through 25.

* T_A is expressed in decibels re 1 microbar per ampere at 1 meter.

** Table 4 gives the results of this test.

It should be noted here that the beam pattern for test 1b is almost identical to that of test 1a and hence is not included. The susceptance curves for all tests are so nearly identical that Figure B4 in Appendix B can be used to represent the susceptance curve for any of the tests performed.

In tests 1a, 1b, and 2, frequency was the only variable. Test 1b was run immediately before the power test and the tension on the mounting bolts holding the flanged triangular ring support was greater than that used in test 1a. Except as indicated, the only difference between tests 1a and 1b, and test 2 was the particular bilaminar disk used. The measured resonant frequency in each case was within 10% of the predicted value. The conductance curves obtained from these tests confirmed that pure resonances were obtained. See Figure 16. It is concluded then, that the triangular ring support is a practical edge support for the water-proofed bilaminar disk.

In test 3 the input power was varied so that the maximum input power could be determined. The unit was operated at 7.5 Kcps. for input power up to and including 10 watts. It was suspected that the bilaminar disk might heat for high input power and hence have its resonant frequency changed. So the unit was allowed to cool and its resonant frequency was found to be 7.3 Kcps. The unit was then operated at 7.3 Kcps. While the input power was gradually increased to 47 watts. At 47 watts, the bottom half of the transmitted signal began to distort on its bottom half cycle. This indicated that the unit was beginning to cavitate. Transmit patterns taken at 5, 10, and 20 watts of input power were almost identical. See Figure 19. The data from this experiment is presented in Table 4.

It appears that this transducer can be operated successfully with 40 watts of input power with an efficiency of at least 13%, corresponding to an acoustic output of at least five watts. After the power tests were completed the transducer's resonant frequency was found to have dropped to 7.2 Kcps, causing the two disks used in the water tests to have essentially the same resonant frequency.

Frequency (Kcps)	Input power (watts)	Efficiency (%)
7.5	0.206	17
"	0.638	15.5
"	2.4	16.2
"	2.89	16.2
"	3.61	15.1
"	4.95	15.1
"	6.0	16.6
"	7.4	17.0
"	9.6	16.2
7.3	1.75	22.4
"	3.42	20.9
"	5.0	15.1
"	10.15	15.1
"	20.0	13.2
"	47.1	13.2

Table 4.

Results of test #3. Determination of maximum input power.

Tests 4 through 7 constituted a single test whereby the effect of varying the rear cavity oil volume could be determined. Physical limitations would not allow the cavity volumes of 1.1π in.³ and 1.3π in.³ to be used. For each cavity volume used, the resonant frequency of the transducer was at least one Kcps less than that observed for the completely filled unit. It is interesting to note that an efficiency of 17.4% was observed in test #7 when the rear cavity volume was $.90 \pi$ in.³. This particular result enhances the possibility of miniaturizing transducer elements by the use of bilaminar disks.

In general, the tension on the mounting bolts was found to have a marked effect on the shape of the conductance curve. For too little tension, double resonances were observed. Increasing the mounting bolt tension eliminated this problem and caused the resonant frequency to increase. However, the increase in resonant frequency with increasing mounting bolt tension tended to level off. So by firmly mounting the disk, the resonant frequency for different disks can be brought in close agreement.

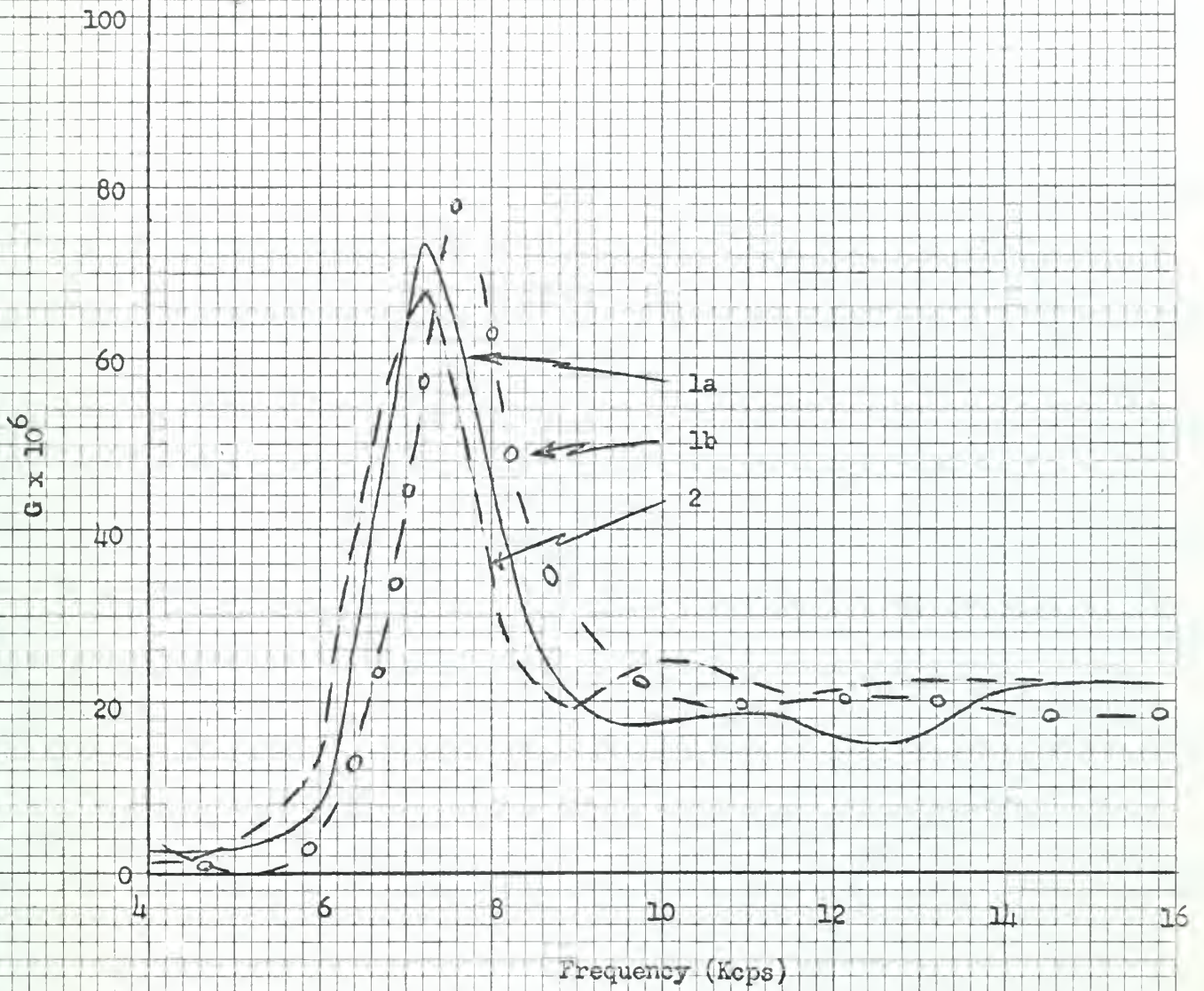


Figure 16. Conductance curves for tests 1a, 1b, and 2.

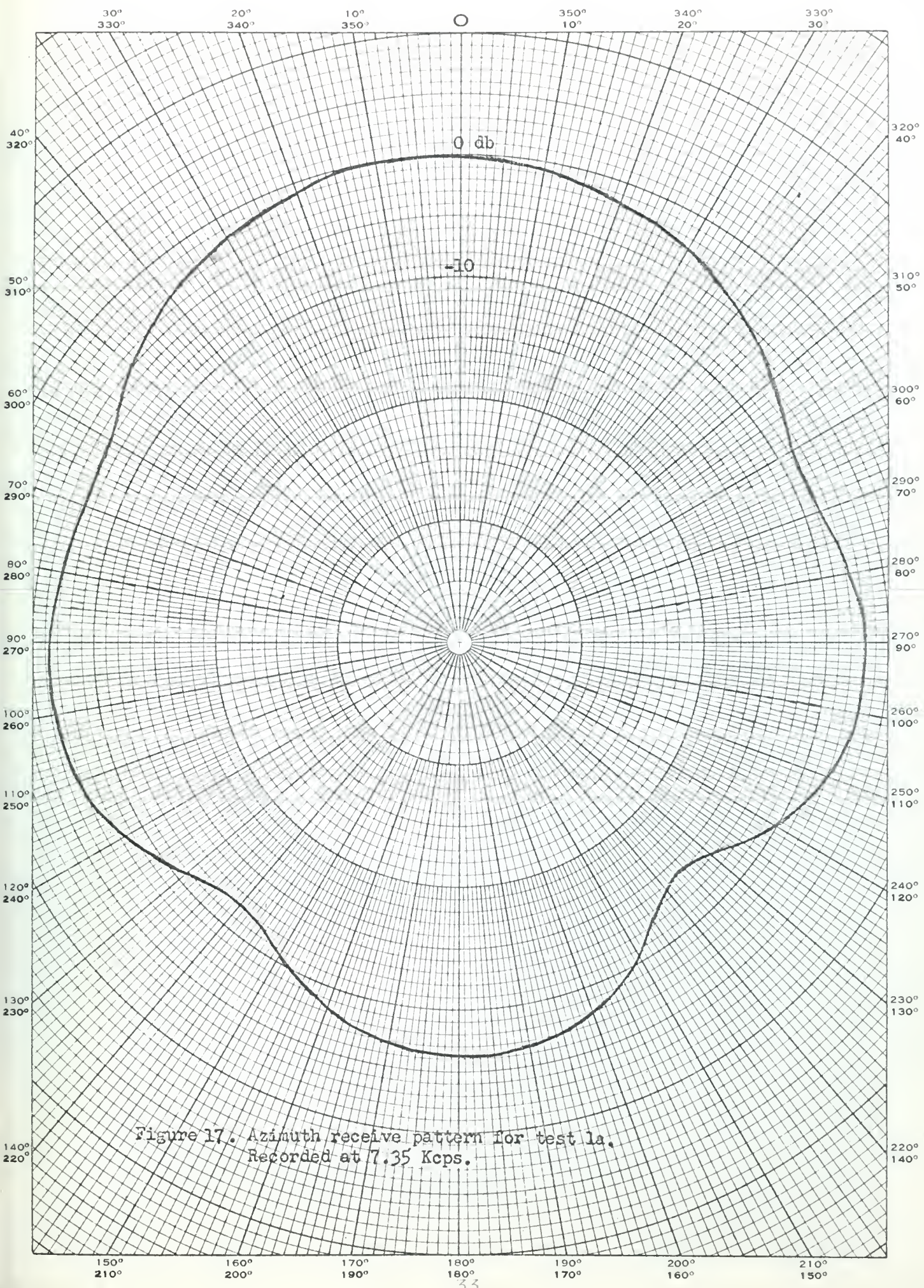


Figure 17. Azimuth receive pattern for test 1a.
Recorded at 7.35 Kcps.

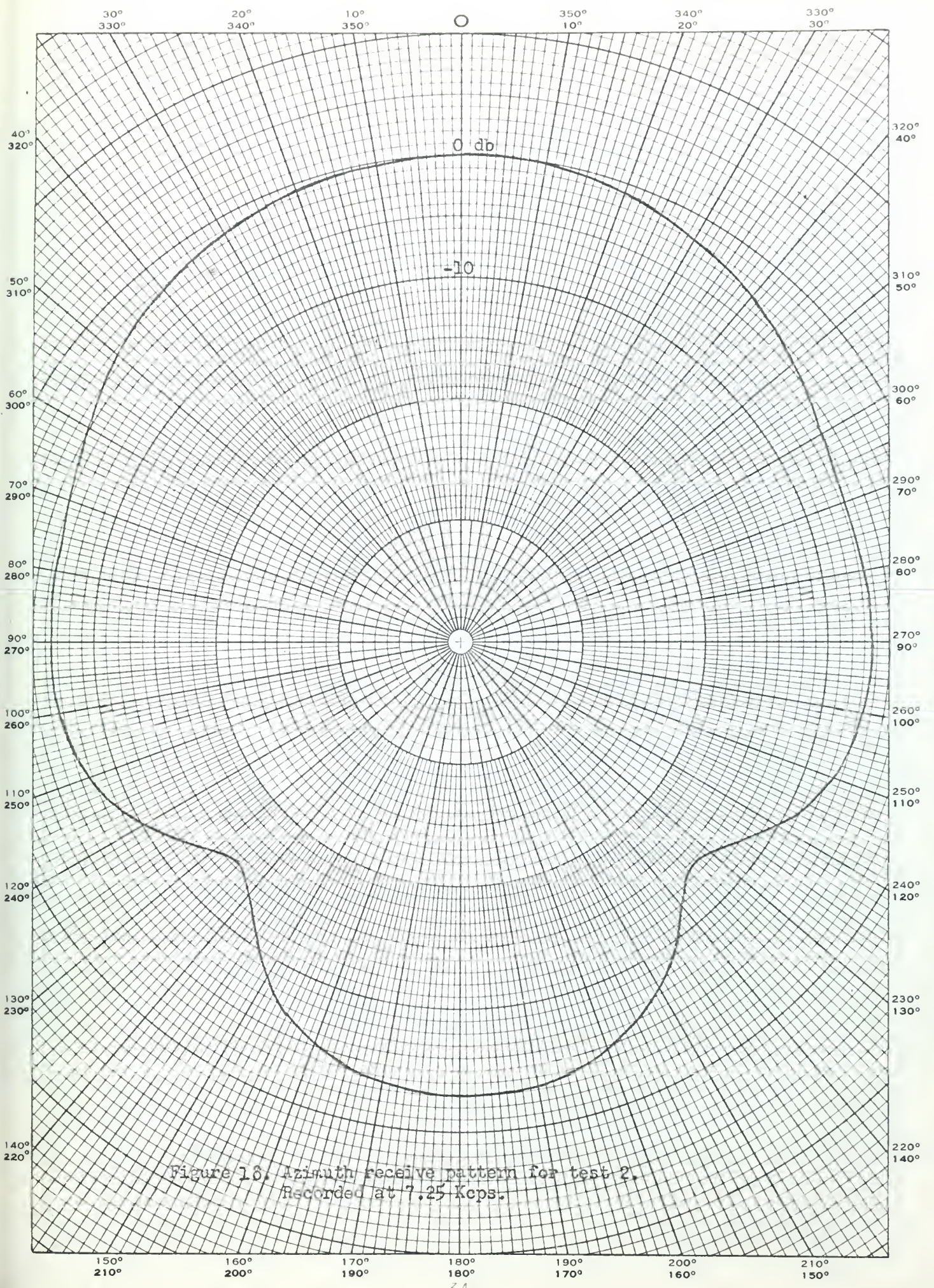


Figure 18. Azimuth receive pattern for test 2.
Recorded at 7.25 Kcps.

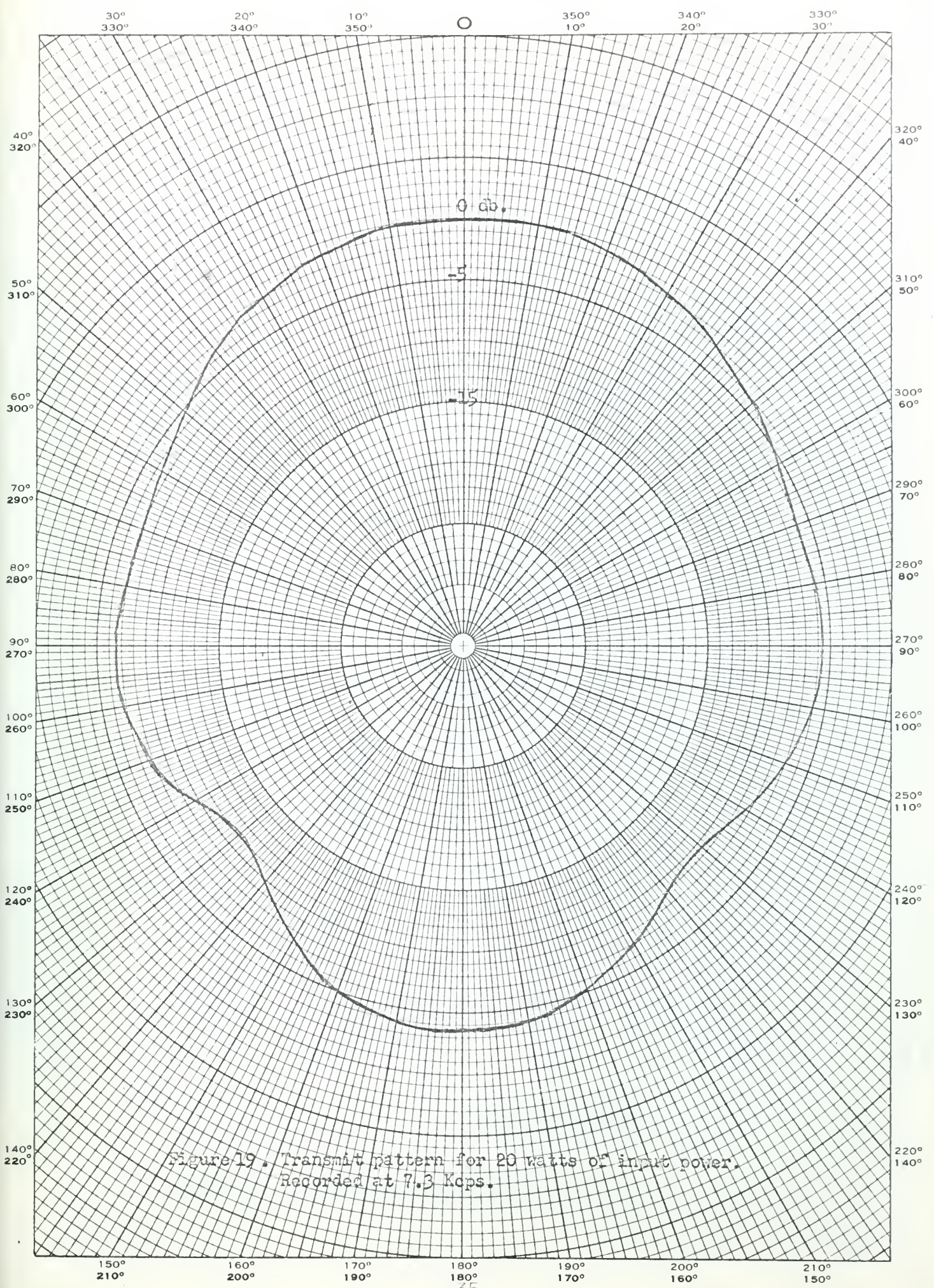


Figure 19. Transmit pattern for 20 watts of input power.
Recorded at 7.3 Kcps.

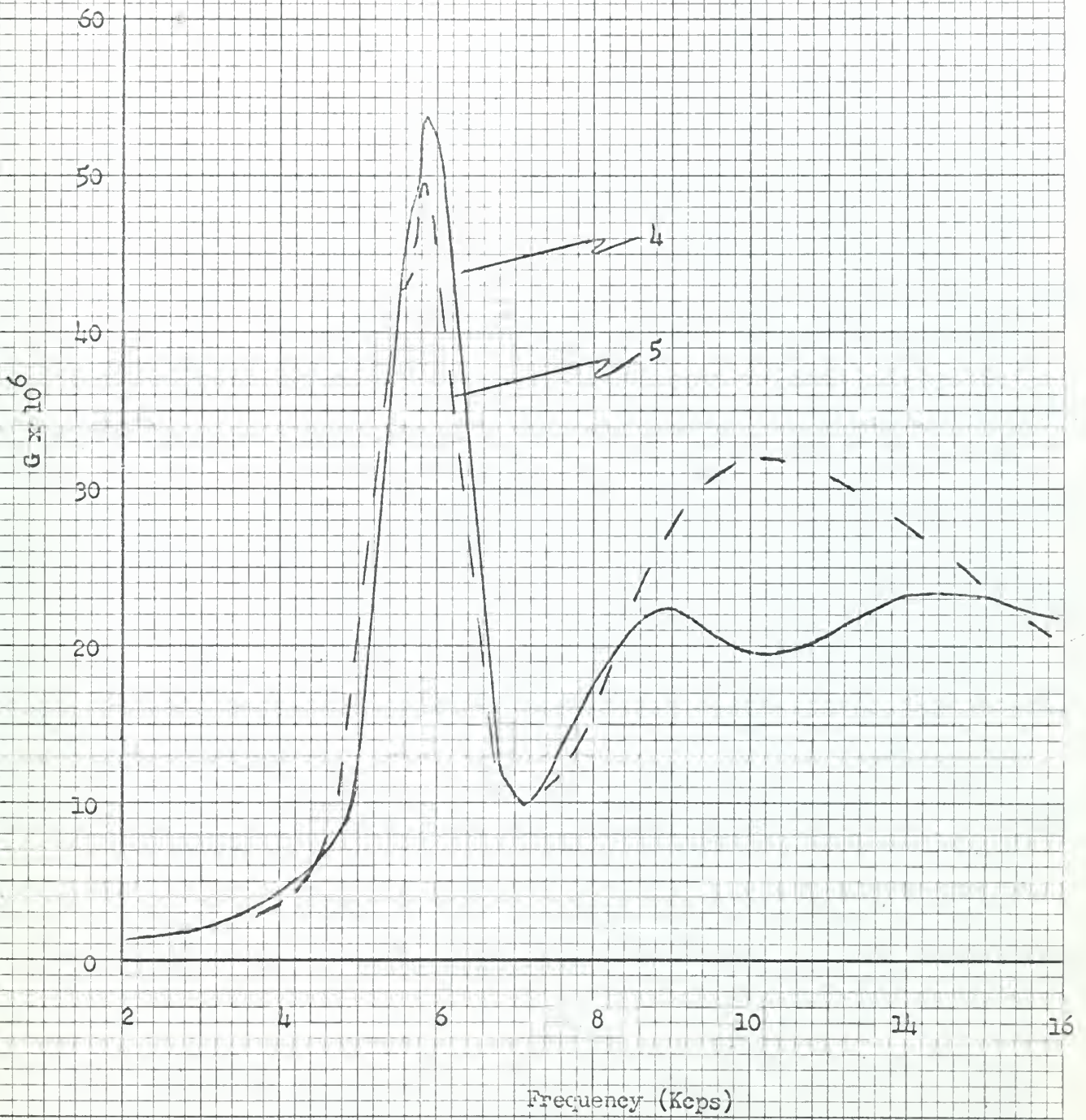


Figure 20. Conductance curves for tests 4 and 5.

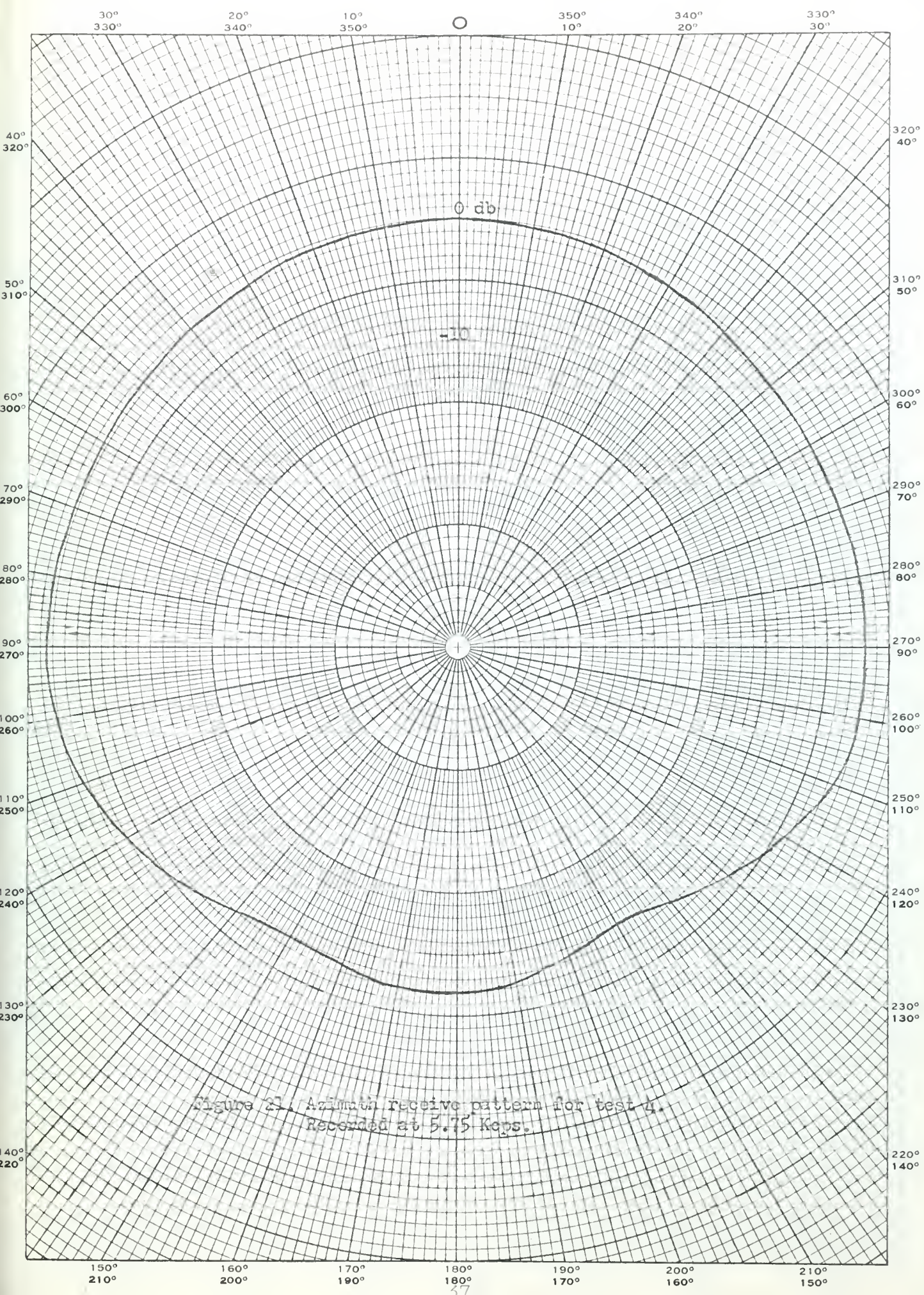


Figure 21. Azimuthal receive pattern for test 4.
Recorded at 5.75 Kcps.

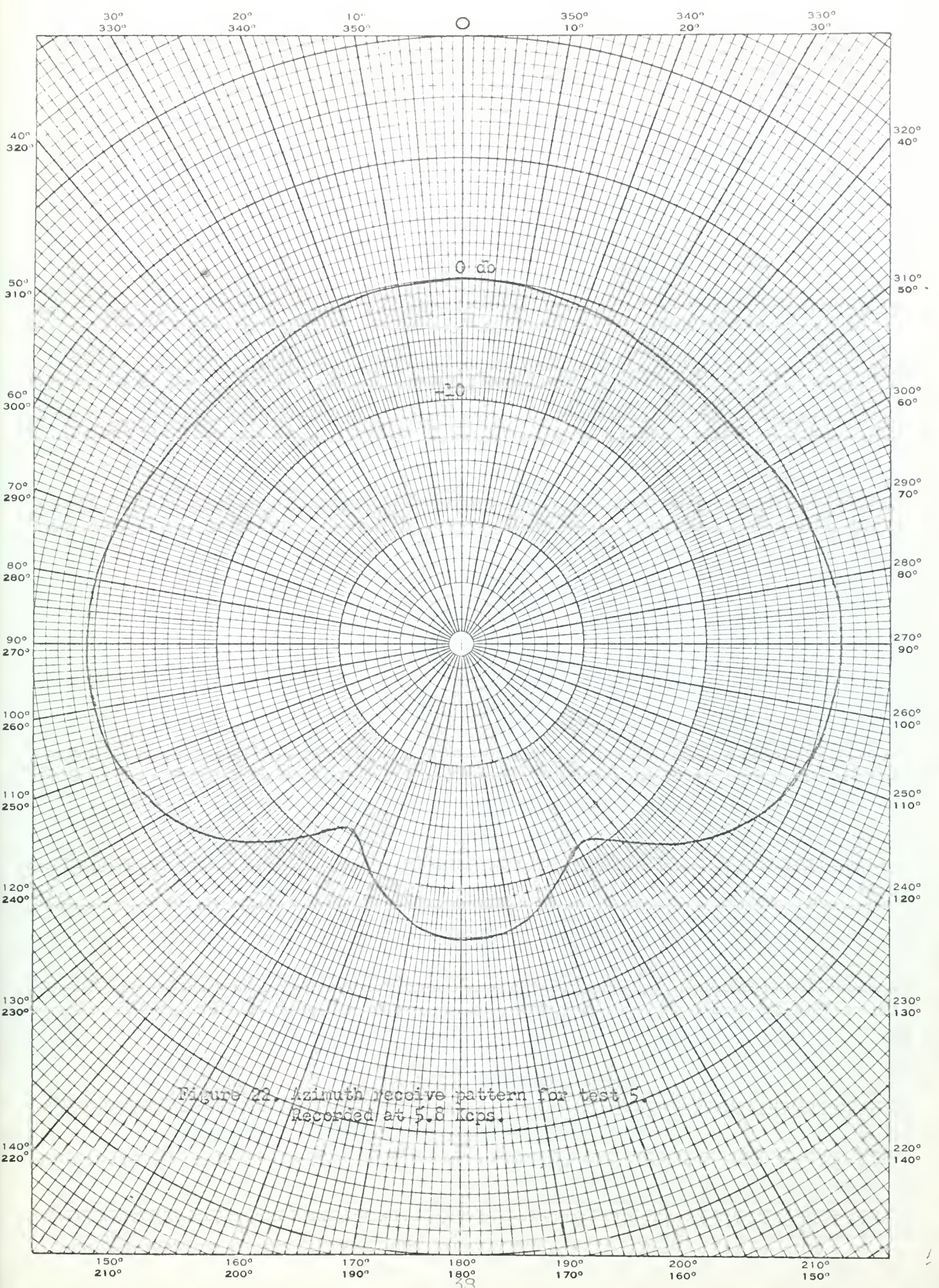


Figure 22 Azimuth receive pattern for test 5
Recorded at 5.8 Mcps.

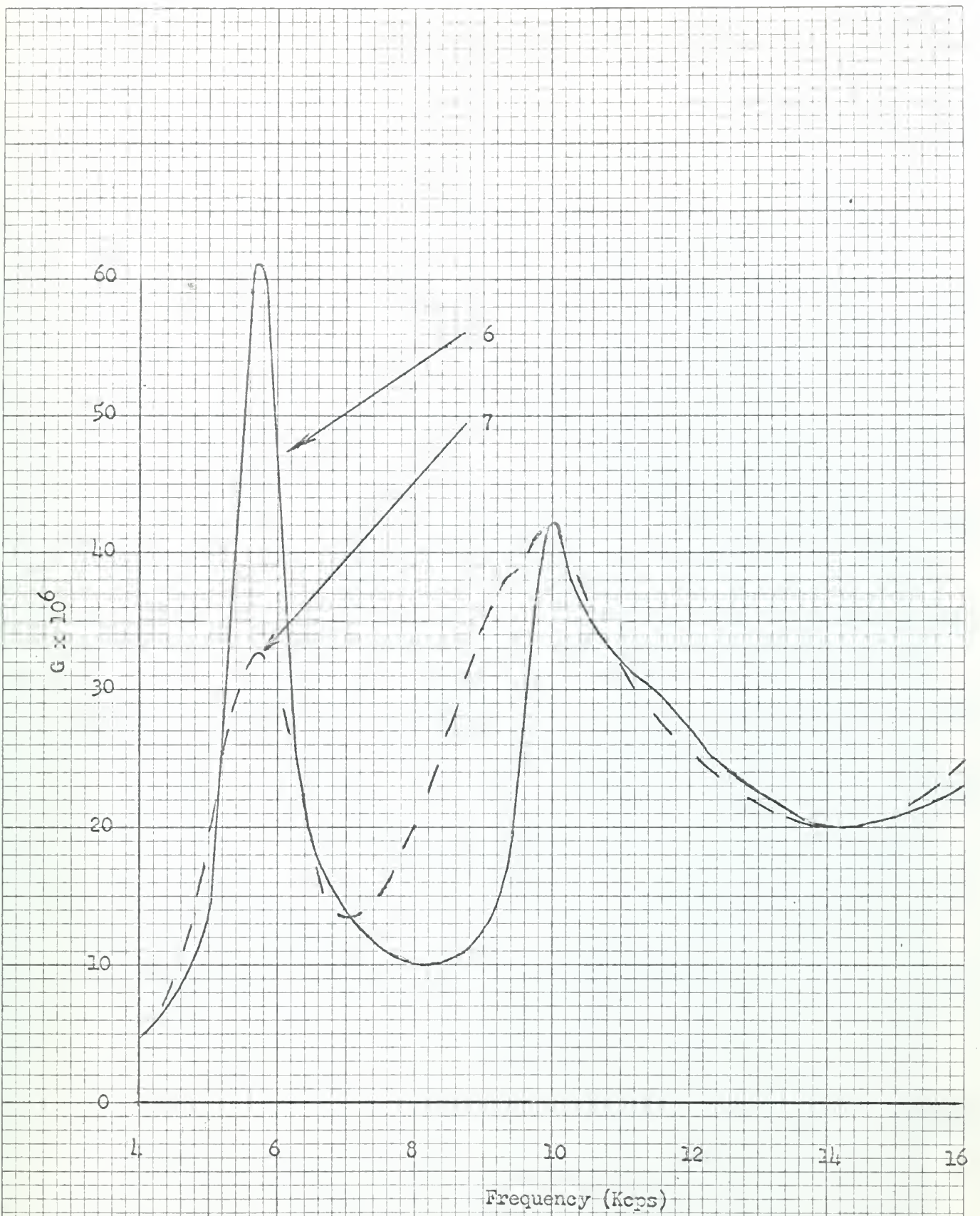
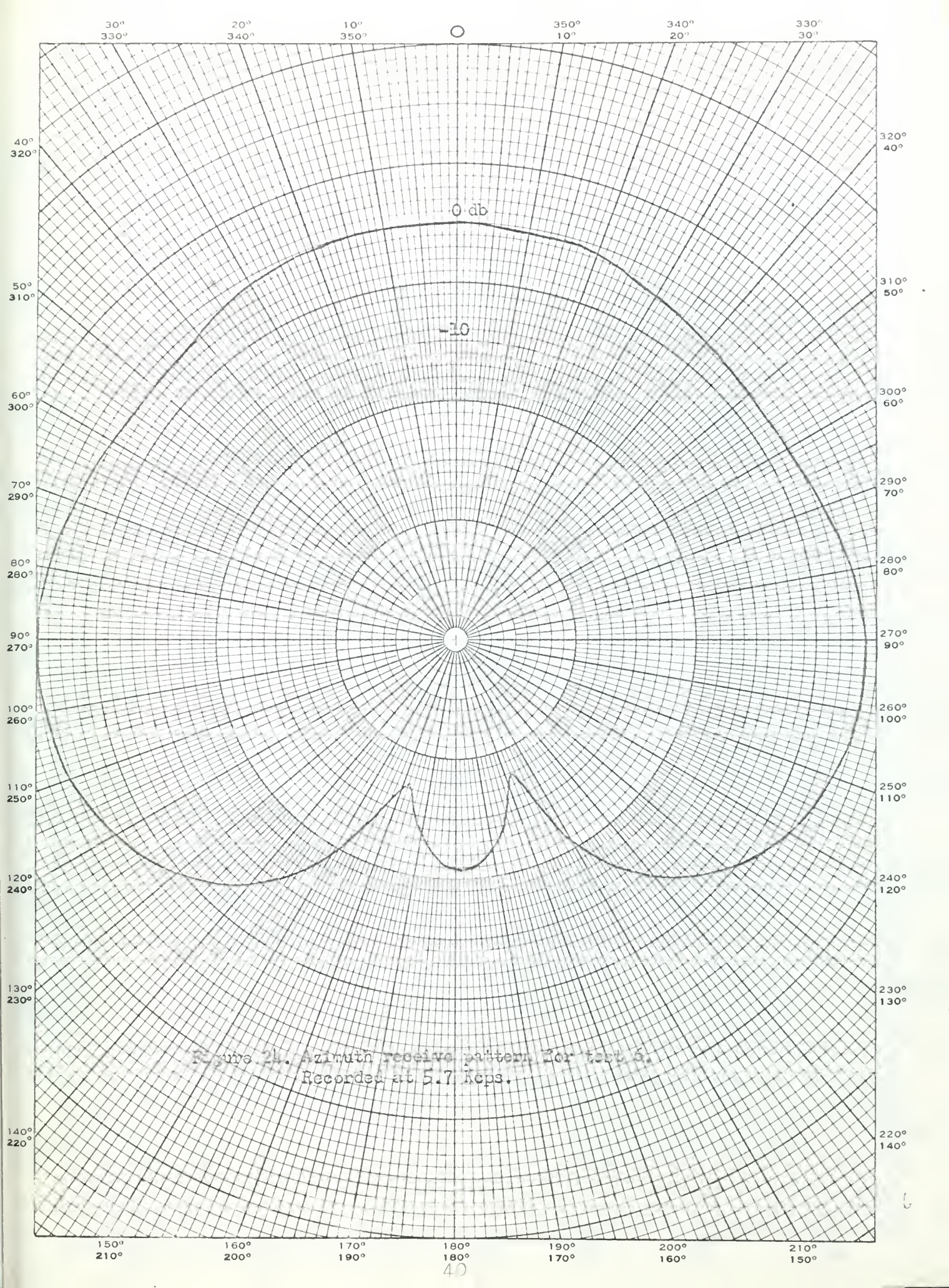


Figure 23. Conductance curves for tests 6 and 7.



Section 10. Conclusion.

The triangular ring supporting device developed in this report was found to be a good approximation to an ideal edge support for a bilaminar disk. While conducting the experiments described in this report, it was determined that the resonant frequency of the bilaminar disk transducer could be predicted with reasonable accuracy by use of the formulae developed in Appendix A.

The mounting structure designed for testing the waterproofed bilaminar disk was completely adequate for the tests performed. This structure was designed so that the pressure on either side of the disk would equalize. Hence, this transducer was not depth limited.

The unit was found to have good power handling capabilities and reasonably good efficiency. This, in conjunction with its mechanical quality factor of 4.5 for the primary design, indicates that the transducer can find some practical use, possibly as a sonobuoy transducer in a submarine/aircraft communication system. In particular, the beam pattern, resonant frequency, bandwidth, depth capability, and power output of the disk transducer indicates that with additional development that it can be used in a torpedo position monitoring system. At its present stage of development, this disk transducer can be used as a small, medium power, laboratory source.

Although the transducer used in the preceding experiments is usable in its present form, many tests should be performed so that the full potential of a bilaminar disk might be realized. First, the thickness to diameter ratio and the diameter of the bilaminar disk should be

varied to determine the range of disk sizes for which the triangular ring supporting device remains a good approximation to an ideal edge support. At the same time, the degree of applicability of the equations presented in Appendix A can be determined. The transducer should be tested at depth to determine the practicality of using the mounting structure as a deep operating unit. Attempts to pre-stress the bilaminar disk should be made to improve its power handling capabilities. Finally, the mounting structure design should be modified so that the outer case is electrically isolated from the bilaminar disk.

The results obtained by varying the rear cavity volume were quite interesting and promising. The reduction in resonant frequency was most likely caused by an increase in the effective mass as seen by the bilaminar disk. At any rate, the reduction in resonant frequency enhances the possibility of miniaturizing transducer elements by the use of bilaminar disks. To further this cause a mounting structure should be designed wherein the rear cavity volume can be minimized. At the same time this design should have the capability of having its rear cavity volume carefully controlled. Such a structure should be tested for its power handling capabilities and for its ability to operate at depth. In the course of such tests the rear cavity oil volume should be varied in order to determine the rear cavity volume which gives the best performance.

BIBLIOGRAPHY

1. American Standards Association, Inc., American Standard Procedures for Calibration of Electroacoustic Transducers, Particularly Those for Use in Water, Dec., 1957
2. Handy, R. J. Theoretical Analysis of Piezoelectric Flexural Disk Transducers, Bendix Pacific Division Report 8920R34, 1962
3. Institute of Radio Engineers, "Standards on Piezoelectric Crystals, 1949, Proceedings of the I. R. E., vol. 37, pp. 1378-1395
4. Kinsler, L. E. and Frey, Fundamentals of Acoustics, John Wiley and Sons, Inc., 1962
5. Lord Rayleigh, The Theory of Sound, 2nd ed., Dover Publications 1945
6. Schenck, H. A. Bilaminar Ceramic Flexural Vibrators, Technical Memorandum No. 59, Acoustics Research Laboratory, Harvard University, Cambridge, Mass., Sept., 1964, Office of Naval Research Contract Nonr-1866(24)
7. Woollett, R. S. Theory of the Piezoelectric Flexural Disk Transducer, with Applications to Underwater Sound, USL Research Report No. 490, December 1960
8. Zilinskas, G. J. Flexural Vibrations in a Piezoelectric Bar, Bendix Pacific Division Report No. 8920R51, March, 1963

APPENDIX A

OUTLINE OF THE ANALYTICAL DESCRIPTION
OF A BILAMINAR DISK TRANSDUCER

The theory in this appendix is outlined from Woollett's paper [7]. His approach is to base the disk analysis on an assumed approximate deflection curve. The accuracy of the assumed curve is judged by comparing the predicted resonant frequency with the observed resonant frequency for the mode of vibration determined by the boundary conditions.

1. Deflection curve.

The assumed deflection curve is a power series. It is expressed in polar coordinates as

$$u(r) = f \left(\alpha_0 + \alpha_1 \frac{r}{a} + \alpha_2 \frac{r^2}{a^2} + \alpha_3 \frac{r^3}{a^3} + \alpha_4 \frac{r^4}{a^4} \right) \quad (A-1)$$

where,

$u(r)$ = the normal displacement of the central surface of the disk,

f = a time varying amplitude factor,

r = the radial coordinate,

a = the radius of the disk, and

$\alpha_0, \alpha_1, \alpha_2, \alpha_3, \alpha_4$ = the deflection curve coefficients, specified by the boundary conditions determined by the disk's mounting.

Specifically, the deflection curve is assumed to be a harmonic time function, hence

$$f = \bar{f} e^{j\omega t} \quad \text{and} \quad \dot{f} = j\omega \bar{f} e^{j\omega t} \quad (A-2)$$

An edge supported disk has the property

$$\left. \frac{du}{dr} \right|_{r=a} = 0,$$

so α_1 must be identically zero. And we can write

$$u(r) = f \left(\alpha_0 + \alpha_2 \frac{r^2}{a^2} + \alpha_3 \frac{r^3}{a^3} + \alpha_4 \frac{r^4}{a^4} \right) \quad (A-3)$$

2. Assumptions.

The assumptions used in the following derivations are:

- the bilaminar disk has a fixed velocity distribution, i.e., as frequency is held constant, the deflection curve is invariant with respect to the driving and loading conditions,
- the disk thickness is very small with respect to its radius,
- the vibration amplitude is very small with respect to the disk's thickness, and
- the bond thickness is negligible.

3. Kinetic energy of the disk.

By assumptions a and b above, rotary inertia and the variation of velocity with thickness are negligible. Hence, the kinetic energy of the disk is given by

$$T_p = \int_{\text{area}} \frac{1}{2} \rho_p b \dot{u}^2(r) dA \quad (\text{A-4})$$

or,

$$T_p = \pi \rho_p b \int_0^a \dot{u}^2(r) r dr$$

Using equations A-2 and A-3, we find that

$$T_p = \frac{1}{2} \pi a^2 b \rho_p \dot{\xi}^2 \mathcal{K} = \frac{1}{2} \pi a^2 b \rho_p \omega^2 \xi^2 \mathcal{K} \quad (\text{A-5})$$

where,

T_p = the total instantaneous kinetic energy of the disk,

b = the disk's thickness,

ρ_p = the density of the disk,

ω = the angular frequency, and

$$\begin{aligned} \mathcal{K} = & \alpha_0^2 + \alpha_0 \alpha_2 + \frac{1}{3} \alpha_2^2 + \frac{4}{5} \alpha_0 \alpha_3 + \frac{4}{7} \alpha_2 \alpha_3 \\ & + \frac{1}{4} \alpha_3^2 + \frac{2}{3} \alpha_0 \alpha_4 + \frac{1}{2} \alpha_2 \alpha_4 + \frac{4}{9} \alpha_3 \alpha_4 + \frac{1}{5} \alpha_4^2 \end{aligned} \quad (\text{A-5a})$$

4. Potential energy of a disk.

The strain (potential) energy of a disk, U , is equal to the work done on the disk by external forces which deforms the disk from its natural state to an equilibrium state characterized by the displacement $u(r)$. In accordance with the I. R. E. standard notation for piezoelectric crystals², the T_{31} , T_{32} , T_1 , and T_2 stresses are required to deform the disk into the shape specified by the deflection curve,

At this point Woollett gives the equations of state for a piezoelectric ceramic material subject to one dimensional bending as

$$T_1 = \frac{\chi_3}{\Delta_{11}^D [1 - (\sigma^D)^2] R_1} - \frac{g_{31} D_3}{\Delta_{11}^D (1 - \sigma^D)} \quad (A-6)$$

$$T_2 = \frac{\sigma^D \chi_3}{\Delta_{11}^D [1 - (\sigma^D)^2] R_1} + \frac{g_{31} D_3}{\Delta_{11}^D (1 - \sigma^D)} \quad (A-7)$$

and,

$$E_3 = \frac{-g_{31} \chi_3}{\Delta_{11}^D (1 - \sigma^D) R_1} + \frac{2 g_{31}^2 D_3}{\Delta_{11}^D (1 - \sigma^D)} + \beta_{33}^T D_3 \quad (A-8)$$

where,

- χ_3 = the rectangular coordinate indicating center displacement,
- g_{31} = the piezoelectric strain constant,
- Δ_{11}^D = compliance modulus at constant electric displacement,
- σ^D = Poisson's ratio of piezoelectric material at constant D_3
- D_3 = electric displacement in the X_3 direction,
- E_3 = the electric field strength in the X_3 direction,
- R_1 = the principal radius of curvature for one dimensional bending, and
- β_{33}^T = the dielectric impermeability at constant stress.

² Institute of Radio Engineers, "Standards on Piezoelectric Crystals, 1949." Proceedings of the I.R.E., vol. 37, pp. 1378 - 1395.

Then, by a superposition of two orthogonal one-dimensional bendings, the equations of state for two-dimensional bending are found to be

$$T_1 = \frac{\kappa_3}{\Delta_{11}^D [1 - (\sigma^D)^2]} \left(\frac{1}{R_1} + \frac{\sigma^D}{R_2} \right) - \frac{g_{31} D_3}{\Delta_{11}^D (1 - \sigma^D)}, \quad (\text{A-9})$$

$$T_2 = \frac{\kappa_3}{\Delta_{11}^D [1 - (\sigma^D)^2]} \left(\frac{1}{R_2} + \frac{\sigma^D}{R_1} \right) - \frac{g_{31} D_3}{\Delta_{11}^D (1 - \sigma^D)}, \quad (\text{A-10})$$

and,

$$E_3 = \frac{g_{31} \kappa_3}{\Delta_{11}^D (1 - \sigma^D)} \left(\frac{1}{R_1} + \frac{1}{R_2} \right) + \beta_{33}^{\Delta_{1,2}} D_3, \quad (\text{A-11})$$

where,

R_1, R_2 = the principal radii of curvature, and

$\beta_{33}^{\Delta_{1,2}}$ = the impermeability for a disk blocked at the edge.

From geometrical considerations, the radii of curvature for the prescribed deflection curve are

$$\frac{1}{R_1} = \frac{F}{a^2} \left(2\alpha_2 + 6\alpha_3 \frac{r}{a} + 12\alpha_4 \frac{r^2}{a^2} \right), \quad (\text{A-12})$$

and,

$$\frac{1}{R_2} = \frac{F}{a^2} \left(2\alpha_2 + 3\alpha_3 \frac{r}{a} + 4\alpha_4 \frac{r^2}{a^2} \right). \quad (\text{A-13})$$

The strain energy density, U_V , is found from the above equations

by
$$U_V = \frac{1}{2} T_1 S_1 + \frac{1}{2} T_2 S_2$$

or,

$$U_V = \frac{\kappa_3^2}{2 \Delta_{11}^D [1 - (\sigma^D)^2]} \left(\frac{1}{R_1^2} + \frac{1}{R_2^2} + \frac{2\sigma^D}{R_1 R_2} \right) - \frac{g_{31} \kappa_3}{2 \Delta_{11}^D (1 - \sigma^D)} \left(\frac{1}{R_1} + \frac{1}{R_2} \right) D_3. \quad (\text{A-14})$$

from which the strain (potential) energy per unit area is

$$U_A = \int_{-b/2}^{b/2} U_V dx_3$$

or

$$U_A = \frac{x_3^2}{2A_{11}^D [1-(\sigma^D)^2]} \left(\frac{1}{R_1^2} + \frac{1}{R_2^2} + \frac{2\sigma^D}{R_1 R_2} \right) - \frac{g_{31} K_3 D_3}{2A_{11}^D (1-\sigma^D)} \left(\frac{1}{R_1} + \frac{1}{R_2} \right) \quad (A-15)$$

The strain energy at constant current, U^I , and at constant voltage, U^E , are now derived since these are physically realizable boundary conditions. This requires an expression for D_3 which may be obtained by integrating equation A-11 with respect to x_3 . The applied voltage, e , so obtained, is set equal to zero. From the resultant expression, the displacement D_3 at constant voltage is determined and the result is substituted into equation A-15. Finally, equation A-15 is integrated over the area of the disk to yield the total instantaneous strain

(potential) energy of the disk at constant voltage as

$$U^E = \frac{2\pi b^2 \int^2}{3a^2 A_{11}^D [1-(\sigma^D)^2]} \left[\Lambda^D - \frac{3}{4} K_p^2 (1+\sigma^D) \left(\frac{1}{2} \alpha_2^2 + \frac{3}{2} \alpha_2 \alpha_3 \right. \right. \\ \left. \left. + \frac{81}{64} \alpha_3^2 + 2\alpha_2 \alpha_4 + \frac{36}{10} \alpha_3 \alpha_4 + \frac{8}{3} \alpha_4^2 \right) \right] \quad (A-16)$$

where,

$$K_p = \text{the planar electromechanical coupling coefficient, and} \\ \Lambda^D = \frac{1+\sigma^D}{2} \alpha_2^2 + \frac{3}{2} (1+\sigma^D) \alpha_2 \alpha_3 + \frac{1}{8} \left(\frac{45}{4} + 9\sigma^D \right) \alpha_3^2 + 2(1+\sigma^D) \alpha_2 \alpha_4 \\ + \left(\frac{21}{5} + 3\sigma^D \right) \alpha_3 \alpha_4 + \left(\frac{10}{3} + 2\sigma^D \right) \alpha_4^2 \quad (A-16a)$$

In a similar fashion U^I , the total instantaneous strain (potential) energy of the disk is found to be

$$U^I = \frac{2\pi b^2 \int^2}{3A_{11}^D [1-(\sigma^D)^2]} a^2 \left[\Lambda^D - \frac{3}{4} K_p^2 (1+\sigma^D) \left(\frac{9}{64} \alpha_3^2 + \frac{6}{10} \alpha_3 \alpha_4 + \alpha_4^2 \right) \right]. \quad (A-17)$$

For convenience in notation the following symbols are defined

$$\Lambda^E = \Lambda^D - \frac{3}{4} k_p^2 (1 + \sigma^D) \left(\frac{1}{2} \alpha_2^2 + \frac{3}{2} \alpha_2 \alpha_3 + \frac{9}{8} \alpha_3^2 + 2 \alpha_2 \alpha_4 + \frac{36}{10} \alpha_3 \alpha_4 + \frac{8}{3} \alpha_4^2 \right) \quad (\text{A-17a})$$

and

$$\Lambda^I = \Lambda^D - \frac{3}{4} k_p^2 (1 + \sigma^D) \left(\frac{9}{8} \alpha_3^2 + \frac{6}{10} \alpha_3 \alpha_4 + \frac{2}{3} \alpha_4^2 \right) \quad (\text{A-17b})$$

5. Derivation of the resonant frequency of the unloaded disk, f_{ra} , the electromechanical coupling coefficient, k , and the blocked electrical energy, U_e^W .

a. Resonant frequency of the unloaded disk, f_{ra} .

The resonant frequency of the unloaded transducer can be derived from the above expressions for the kinetic and potential energies by equating their time averages. By using Λ^I or Λ^E in the potential energy expression, the resonant frequency under constant current or constant voltage can be determined. Using Λ to represent Λ^I or Λ^E depending on the driving conditions, and performing the prescribed operations, we get

$$f_{ra} = \frac{b}{\pi a^2} \left(\frac{\Lambda}{3K \alpha_{11}^D [1 - (\sigma^D)^2] \rho_p} \right)^{1/2}$$

or

$$f_{ra} = \frac{1}{\pi} \frac{b c_p}{a^2} \left(\frac{\Lambda}{3K} \right)^{1/2} \quad (\text{A-18})$$

where,

$$c_p = [\alpha_{11}^D (1 - \sigma^D)^2]^{-1/2} \rho_p, \text{ which is the sound velocity of extensional waves in an infinitely extended medium.}$$

b. Electromechanical coupling coefficient, k .

Woollett's definition of the electromechanical coupling coefficient is

Let the transducer structure be displaced into the configuration

of the mode for which k is to be determined, and the amplitude of the displacements be the same² for both open-circuit and short circuit conditions. Then k^2 is the ratio of (1) the difference in mechanical energy required under open-circuit and short circuit conditions to establish the specified displacements to (2) whichever of these mechanical energies is the greater.

From this definition we can write

$$k^2 = 1 - \frac{U^E}{U^I}$$

And using equations A-16 and A-17, this expression becomes

$$k^2 = \frac{\frac{3}{4} k_p^2 \frac{\frac{1}{2}(1+\sigma^D)(\alpha_2 + \frac{3}{2}\alpha_3 + 2\alpha_4)^2}{\Delta^D - \frac{3}{4} k_p^2 (1-\sigma^D)(\frac{7}{64}\alpha_3^2 + \frac{6}{10}\alpha_3\alpha_4 + \frac{2}{3}\alpha_4^2)}}{\quad} \quad (\text{A-19})$$

c. Blocked electrical energy, U_e^W .

By integrating equation A-11 with respect to x_3 , and setting

$R_1 = R_2 = \infty$, we obtain the blocked electric displacement as

$$D_3 = \frac{2\ell}{b\beta_{33}^{A,12}} \quad (\text{A-20})$$

where,

ℓ = the applied potential, and

$\beta_{33}^{A,12}$ = impermeability for a plate blocked at its edges.

D_3 is now constant throughout the material, so the blocked electrical energy of the transducer is given by

$$U_e^W = \int_V \frac{1}{2} \beta_{33}^{A,12} D_3^2 dV = \frac{1}{2} \pi a^2 b \beta_{33}^{A,12} D_3^2$$

and since³,

$$\beta_{33}^{A,12} = \beta_{33}^T / (1 - k_p^2)$$

³ Woollett, R. S. op. cit. pp. 64-65

we have

$$U_e^w = \frac{2\pi a^2 (1-k_p^2) e^2}{b \beta_{33}^T} \quad (\text{A-21})$$

where,

β_{33}^T = dielectric impermeability at constant stress.

6. Equivalent circuit of the bilaminar disk transducer.

In this analysis the disk is assumed to have a fixed velocity distribution. It can be represented by the usual equivalent circuit in which the radiating face is characterized by a single velocity, v . Figure A1 represents a suitable equivalent circuit incorporating the assumptions that the deflection curve is independent of frequency and that the disk is conservative. Resistive terms are not included in this circuit since their position and values are best determined by experiment.

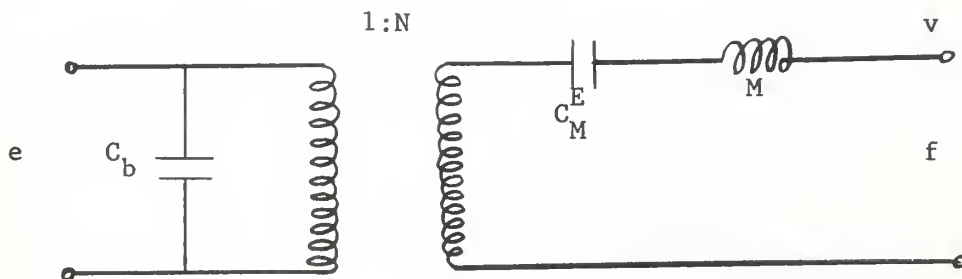


Figure A1
Electromechanical circuit of the disk.

The face velocity has a radial distribution $\dot{u}(r)$. As a convenience, a value of $\dot{u}(r)$ is chosen as the reference velocity, v , so that when v is multiplied by the area of the disk, the volume velocity is obtained. The expression for $\dot{u}(r)$ is obtained by taking the time derivative of equation A-3.

Symbolically,

$$v A_1 = \int_{A_1} \dot{u}(r) dA_1 = \int_0^a \left(\alpha_0 + \alpha_2 \frac{r^2}{a^2} + \alpha_3 \frac{r^3}{a^3} + \alpha_4 \frac{r^4}{a^4} \right) 2\pi r dr \quad (\text{A-22})$$

where,

A_1 = the disk's area.

Carrying out the indicated integration yields

$$v = H^{1/2} \left\{ \right. \quad (\text{A-23})$$

where,

$$H^{1/2} = \left(\alpha_0 + \frac{\alpha_2}{2} + \frac{2}{5} \alpha_3 + \frac{\alpha_4}{3} \right) \frac{\pi}{A_1} . \quad (\text{A-23a})$$

The kinetic energy expressed in terms of the reference velocity is obtained from equations A-5 and A-23 is

$$T_p = \frac{1}{2} \pi a^2 b \rho_p \frac{K}{H} v^2 . \quad (\text{A-24})$$

and the mass, M , referred to this velocity is

$$M = \pi a^2 b \rho_p \frac{K}{H} \quad (\text{A-25})$$

Similarly, the potential energy at constant voltage, U^E , can be written

$$U^E = \frac{2\pi b^3 \Lambda^E u_{av}^2}{3 \epsilon_{11}^D [1 - (\sigma^D)^2] a^2 H} \quad (\text{A-26})$$

where,

$$u_{av} = v/j\omega$$

And the compliance at constant voltage referred to this displacement is

$$C_M^E = \left(\frac{d^2 U^E}{d u_{av}^2} \right)^{-1} = \frac{3 \epsilon_{11}^D (1 + \sigma^D) a^2 H}{4\pi b^2 \Lambda^E} \quad (\text{A-27})$$

By use of equation A-21 for U_e^W , and by a similar technique, we obtain

$$C_B = \frac{4\pi a^2 (1 - k^2)}{b \beta_{33}^T} \quad (A-28)$$

Finally, an expression for N is found from the general relation

$$\frac{k^2}{1 - k^2} = \frac{N^2 C_M^E}{C_B} \quad (A-29)$$

Using the above expressions for C_M^E , and C_B , we find that

$$N = \frac{2\pi g_{31} b (\alpha_2 + \frac{3}{2} \alpha_3 + 2\alpha_4)}{g_{11}^D (1 - \alpha^D) \beta_{33}^{2,12} H^{1/2}} \quad (A-30)$$

7. Determination of the resonant frequency for the loaded bilaminar disk transducer, f_{rw} .

By a detailed derivation, too lengthy to include here, Woollett determines the kinetic energy in the near field of a single transducer, T_w , as

$$T_w = \frac{4}{3} \rho_w a^3 \dot{\theta}^2 = \frac{4}{3} \rho_w a^3 \omega^2 \theta^2 = \frac{4}{3} \rho_w a^3 \frac{\theta}{H} v^2 \quad (A-31)$$

where,

ρ_w = the density of water

$$\theta = \alpha_0^2 + .93333\alpha_0\alpha_2 + .73036\alpha_0\alpha_3 + .59810\alpha_0\alpha_4 + .23810\alpha_2^2 + .38110\alpha_2\alpha_3 + .15358\alpha_3^2 + .31704\alpha_2\alpha_4 + .25688\alpha_3\alpha_4 + .10788\alpha_4^2 \quad (A-31a)$$

Then, f_{rw} , for a loaded disk in an infinite baffle is found by adding the kinetic energy of the water to the kinetic energy of the disk (T_p is given in equation A-4). The total kinetic energy is time averaged and equated to the time averaged potential energy (U is

given by equation A-16 or A-17). This procedure yields f_{rw} as

$$f_{rw} = f_{ra} \left(1 + \frac{8a \rho_w \theta}{3\pi b \rho_p R} \right)^{-1/2}, \quad (\text{A-32})$$

where f_{ra} is the resonant of the unloaded disk as given by equation A-18.

8. Determination of the deflection curve coefficients.

Specification of the boundary conditions allows the determination of the deflection curve coefficients, $\alpha_0 \dots \alpha_4$. From these, the various constants defined in the preceding sections of this report can be evaluated.

For a supported edge disk it is required that the normal displacement and the stress couple vanish at the edge of the disk. This first condition requires that

$$(\alpha_0 + \alpha_2 + \alpha_3 + \alpha_4)_{r=a} = 0, \quad (\text{A-33})$$

and the second requires that

$$\int_{-b/2}^{+b/2} T_1 x_3 dx_3 \Big|_{r=a} = 0. \quad (\text{A-34})$$

Using equation A-9 for T_1 and equations A-12 and A-13 for R_1 and R_2 as required by equation A-34, we find

$$\left[\frac{1}{R_1} + \frac{\alpha^D}{R_2} \right]_{r=a} = \frac{\gamma}{a^2} \left[2(1+\alpha^D)\alpha_2 + 3(2+\alpha^D)\alpha_3 + 4(3+\alpha^D)\alpha_4 \right] = 0 \quad (\text{A-35})$$

Then by setting α_2 or α_3 equal to zero, and setting α_0 equal to one, equations A-33 and A-35 can be solved for the remaining coefficients.

However, Woollett, using Rayleigh's Principle^{4,5}, derives a more accurate deflection curve using all four coefficients. Applying this principle requires the determination of a value for α_2 which minimizes f_{ra} as given by equation A-18. From equation A-18 it is seen that f_{ra} is directly proportional to $\sqrt{\frac{\Lambda}{\kappa}}$. Thus minimizing $\frac{\Lambda}{\kappa}$, will minimize f_{ra} . So by evaluating

$$\frac{d}{d\alpha_2} \left(\frac{\Lambda}{\kappa} \right) = 0$$

for α_2 yields

$$\alpha_2 = -1.4417.$$

Using this value for α_2 and setting $\alpha_0 = 1$, equations A-33 and A-35 are solved to give

$$\alpha_3 = .3304 \quad \text{and} \quad \alpha_4 = .1112.$$

These values for the deflection curve coefficients are used in preparing Appendix C.

8. Determination of f_{ra} for an unloaded, freely vibrating disk.

Rayleigh⁶ gives the boundary conditions for a free disk as

$$\frac{d}{dr} \left(\frac{d^2}{dr^2} u(r) + \frac{1}{r} \frac{d}{dr} u(r) \right)_{r=a} = 0$$

and

$$\left(\frac{d^2}{dr^2} u(r) + \frac{\alpha^b}{r} \frac{d}{dr} u(r) \right)_{r=a} = 0$$

Handy⁷ applies these conditions and obtains

$$f_{ra} = \frac{.352b}{a^2} \left(\frac{\rho_p}{\rho_d} \right) \quad (\text{A-36})$$

⁴ Ibid. pp. 69-70

⁵ Lord Rayleigh, The Theory of Sound, 2nd ed., Dover Publications, New York, 1945

⁶ Ibid.

⁷ Handy, R. J. Theoretical Analysis of Piezoelectric Flexural Disk Transducers, Bendix Pacific Division Report 8920R34, 1962

where,

ρ_{ϕ} = the effective density of the bilaminar disk.

For purposes of this report $\rho_p \doteq \rho_{\phi}$, hence

$$f_{ra} = \frac{.352 b c p}{a^2} \quad (\text{A-37})$$

is accurate enough for this report.

APPENDIX B

Sample Calculations

The equations and technique used here for determining the directivity index and efficiency is as described in reference [1].

The directivity factor, R_{θ} , is the ratio of the mean square pressure at some fixed distance and specified direction, to the mean square pressure at the same distance averaged over all directions. The reference distance must be great enough to allow spherical divergence, i. e., far field. Three meters was used as a reference distance in these experiments. The reference direction was taken as that of maximum response.

Symbolically,

$$R_{\theta} = \frac{4\pi r^2 p_a^2}{\int_{\text{sphere}} p^2(\phi, \theta) dS}$$

or,

$$R_{\theta} = 4\pi \left\{ \int_0^{\pi} \int_0^{2\pi} \left[\frac{p(\phi, \theta)}{p_a} \right]^2 \sin\theta d\theta d\phi \right\}^{-1} .$$

where, $p(\phi, \theta)$ = the sound pressure as a function of direction at some fixed distance,

p_a = the sound pressure in the reference direction at the same distance,

r = the radius of a sphere whose center is the effective acoustic center of the source, and

dS = the element of area on the surface of the sphere.

However, for practical transducers, $p(\phi, \theta)$ is not readily available.

But for a circular piston transducer, we can write

$$R_{\theta} = 4\pi r^2 p_a^2 / \int_0^{\pi} 2\pi r^2 p^2(\theta) \sin\theta d\theta .$$

In this case $f(\theta)$ is generally unknown. But since the area of a circular sector of a sphere is proportional to the angle measured from the reference direction, a plot of pressure squared versus sector area can be integrated with a planimeter to give R_θ . A convenient method to use for this calculation is given in Appendix 7 of the above mentioned reference. Figure (B2) is an actual plot p^2 versus θ taken from the azimuth receive pattern shown in figure (B1). By this technique

$$R_\theta = \frac{2 \times \text{Area of chart}}{\text{Area under curve}} = \frac{99}{31.4} = 3.16$$

At this point it is convenient to define Directivity Index (DI) and the transmitting current response (S_0). The defining equations are:

$$DI = 10 \log_{10} R_\theta, \text{ and,}$$

$$S_0 = \frac{Pa}{I_D} \quad (\text{microbars at 1 meter/ampere})$$

where,

$$I_D = \text{the current into the transducer.}$$

The transmitting efficiency is given by

$$\eta = \frac{4\pi r^2}{R_\theta} \cdot \frac{Pa^2}{\rho_0 c} \cdot \frac{10^{-3}}{I_D^2 R_S}$$

where, R_S = the series resistance of the transducer measured on an a/c bridge, and

$\rho_0 c$ = the characteristic impedance of the loading medium.

And to facilitate computation

$$\eta_{dB} = 10 \log_{10} \eta = -(70.9 + 10 \log_{10} R_S + DI) + T_A$$

where,

$$T_A = 20 \log_{10} \frac{Pa}{I_D}$$

Since 25 feet of Beldon #8422 coaxial cable was connected to the transducer, its capacitance, C_C , is in parallel with the transducer's capacitance, C_D . The measured T_A then, includes the current through C_C . To cancel this effect, $20 \log_{10} (1 + C_C/C_D)$ must be added to the measured T_A . This correction factor is easily derived from basic circuit theory.

Parallel resistance and reactance were measured on a bridge. Their dual series resistance R_S , and series reactance X_S , are found from the following conversion formulae:

$$R_S = R_P / (1 + Q_E^2), \quad X_S = \frac{X_P Q_E^2}{1 + Q_E^2} \quad \text{where, } Q_E = \frac{R_P}{X_P}$$

The value of R_S so determined is then used in the calculation of efficiency.

Finally, η_{db} is given by

$$\eta_{db} = - [70.9 + 10 \log_{10} R_S + DI] + T_A + 20 \log_{10} [1 + C_C/C_D].$$

From the experimental data and the above formulae we have the following values:

$$DI = 5.5, \quad T_A = 93.6, \quad R_P = 14,600 \text{ ohms}, \quad X_P = 1,947 \text{ ohms},$$

$$R_S = 255 \text{ ohms}, \quad C_D = 11,273 \text{ pf.}, \quad C_C = 750 \text{ pf.}, \quad \text{and } C_C/C_D = .067.$$

From which $\eta_{db} = -6.3$ or $\eta = 23.4\%$.

For reference, the conductance and susceptance curves obtained from the experiment used for this sample calculation are shown in figures (B3) and (B4), respectively.

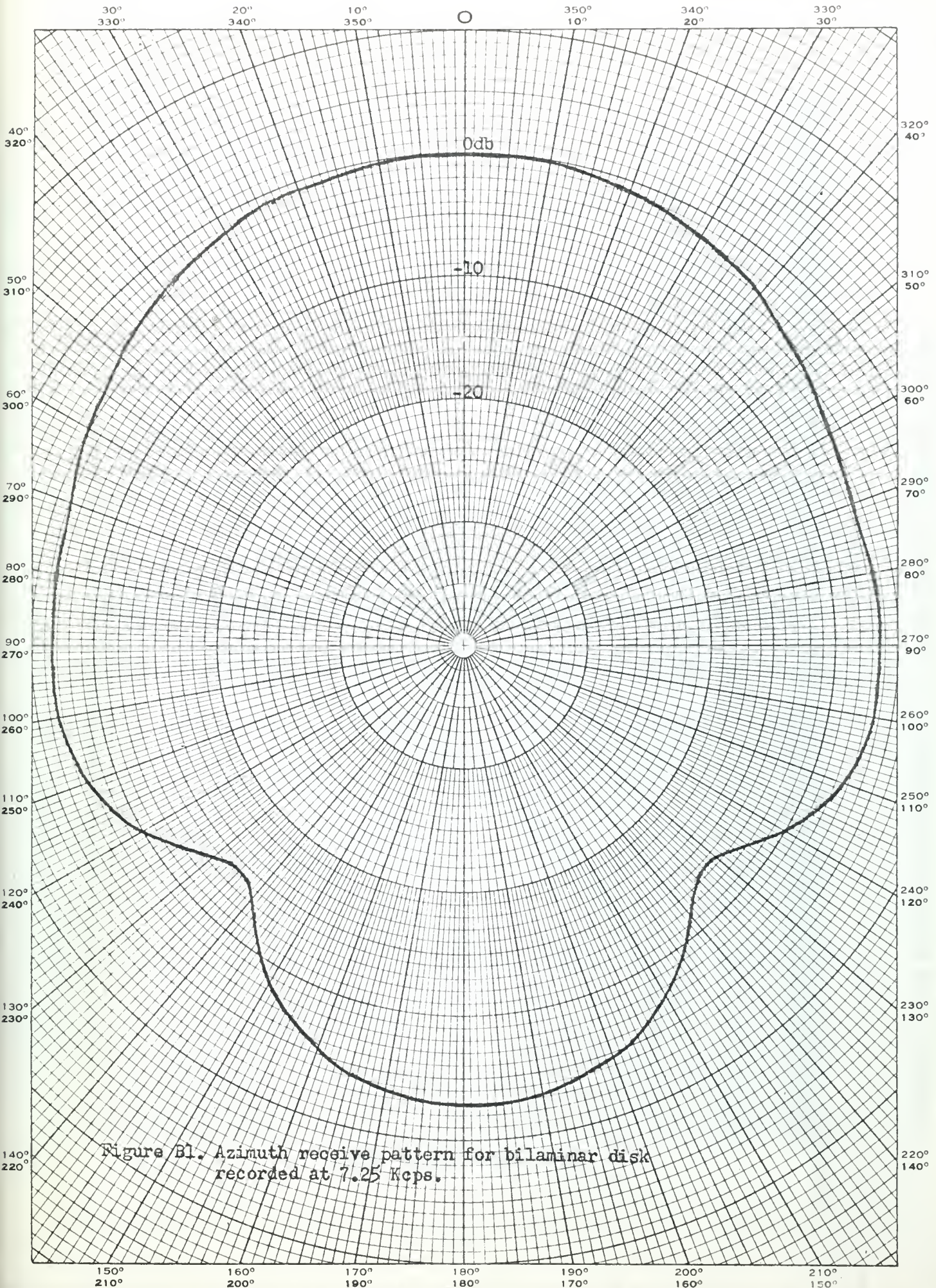


Figure B1. Azimuth receive pattern for bilaminar disk recorded at 7.25 Kcps.

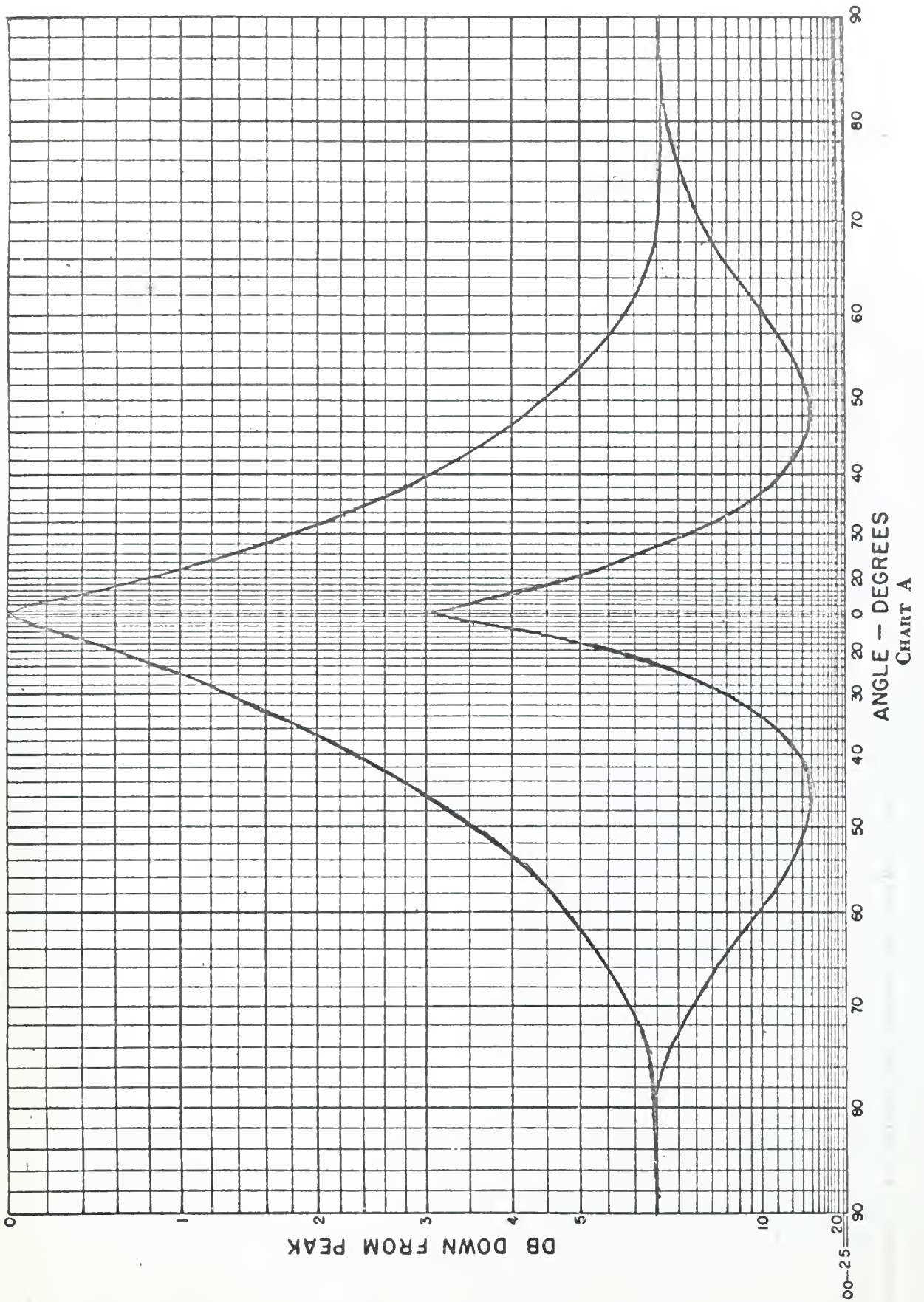


Figure B2. Plot of p^2 versus θ (Required for obtaining the directivity index).

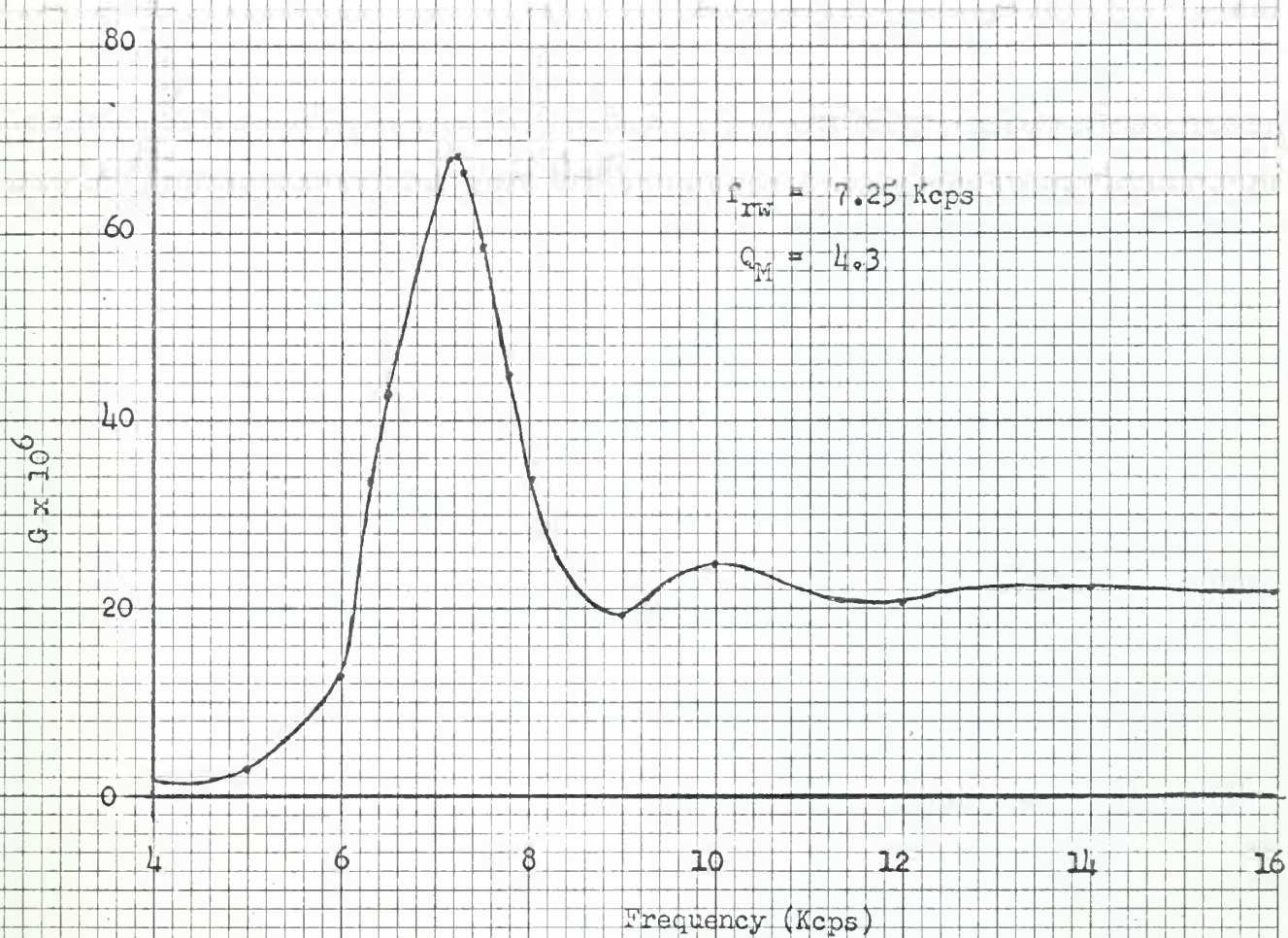


Figure B3. Conductance curve for the bilaminar disk transducer

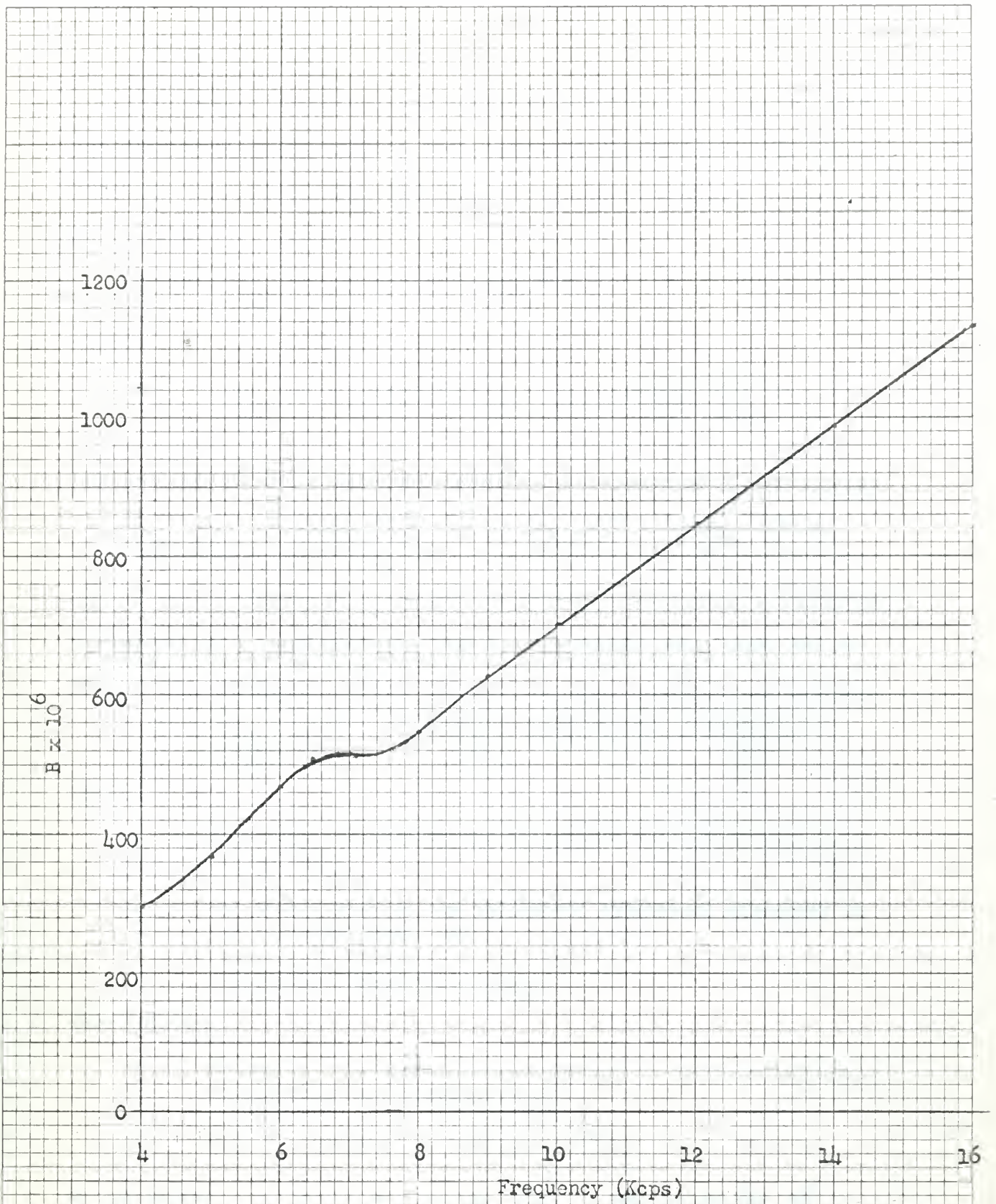


Figure B4. Susceptance curve for the bilaminar disk transducer.

The equipment used for the determination of R_S could not be used for high input power (greater than 2 watts). To determine efficiency for high input power, the efficiency formula derived above is modified as follows

$$\text{we had, } \eta_{db} = -[70.9 + 10 \log_{10} R_S] + T_A$$

$$\text{or, } \eta_{db} = -[70.9 + DI] + T_A + 10 \log_{10} \frac{1}{R_S}$$

The last two terms in the right member of this equation can be written

$$10 \log_{10} \frac{1}{R_S} + 10 \log \frac{P_a^2}{I_D^2} = 10 \log_{10} P_a^2 - 10 \log_{10} I_D^2 R_S$$

P_a can be determined by measuring the pressure field with a calibrated hydrophone at a known distance from the transducer under test and referring this measured pressure back to the test transducer as follows:

$$10 \log_{10} P_a^2 = 20 \log_{10} [E_s / S_s] + 20 \log_{10} d,$$

where,

E_s = the output voltage of the calibrated hydrophone expressed in rms volts,

S_s = the sensitivity of the calibrated hydrophone expressed in rms volts/microbar, and

d = separation expressed in meters.

Then letting,

M_s = $20 \log S_s$, the sensitivity expressed in decibels referenced to one volt rms/ microbar, and

E'_s = $2 \cdot 2^{\frac{1}{2}} E_s$, the peak to peak value of E_s

we can write, $10 \log_{10} P_a^2 = 20 \log_{10} \frac{E'_s}{2.828} - M_s + 20 \log_{10} d.$

Next, it is noted the $I_D^2 R_S$ is the power dissipated by the transducer. It can be determined by measuring the voltage across the transducer, the current into the transducer, and the phase angle between the two. Hence,

$$I_D^2 R_S = I_D E_D \cos \psi$$

where,

I_D = the current into the transducer expressed in rms amperes,

E_D = the voltage across the transducer expressed in rms volts,
and

ψ = the phase angle between I_D and E_D .

Letting I_D' and E_D' represent the peak to peak values of I_D and E_D , we write

$$I_D^2 R_S = \frac{I_D' E_D'}{8} \cos \psi$$

So by these substitutions for P_a^2 and $I_D^2 R_S$, the efficiency can be written as

$$\eta_{db} = -(70.9 + DI + M + 10 \log \frac{I_D' E_D' \cos \psi}{8}) + 20 \log \frac{E_S}{2.828} + 20 \log d$$

Finally, the mechanical quality factor Q_M , is measured as follows

$$Q_M = f_{rw} / (f_2 - f_1)$$

where,

f_{rw} = frequency of maximum conductance, and

f_2, f_1 = the frequencies on either side of f_{rw} where the conductance is one half of its peak value.

APPENDIX C

MATERIAL PROPERTIES OF BaTiO_3 (5% CaTiO_3 additive) AND SUMMARY OF FORMULAE AND CONSTANTS FOR THE SUPPORTED EDGE BILAMINAR DISK TRANSDUCER.

1. Material properties.

Property	Units	Dimension
C_p	m/sec	4900
ρ_p	kg/m^3	5500
R_p		.325
g_{31}	$\text{m}^2/\text{coul.}$	5.41×10^{-3}
β_{33}^T	volt-m/coul.	9.41×10^7
$\beta_{33}^{2,2}, \beta_{33}^{2,2}$	volt-m/coul.	1.05×10^8
d_{11}^D		8.31×10^{-12}
σ^D		0.3

2. Formulae and Constants.

$$\begin{aligned} \kappa &= .2832 && \text{(A-5a)} \\ \kappa^D &= .4316 && \text{(A-16a)} \\ \kappa^E &= .3997 && \text{(A-17a)} \\ f_{ra}^E &= 1070 b/a^2 && \text{(A-18)} \\ k &= .769 R_p (1 - .1031 R_p^2)^{-1/2} && \text{(A-19)} \\ H &= .2011/a^2 && \text{(A-23a)} \\ \Theta &= .2523 && \text{(A-31a)} \\ f_{rw} &= f_{ra} (1 + .140 a/b)^{-1/2} && \text{(A-32)} \end{aligned}$$

thesY77

The design and development of a practica



3 2768 001 90557 3
DUDLEY KNOX LIBRARY